Title: The distribution of platinum-group elements and Te, As, Bi, Sb and Se (TABS+) in the Paraná Magmatic Province: Effects of crystal fractionation, sulfide segregation and magma degassing

Authors: *Eduardo Mansur[1]; Sarah-Jane Barnes[1]; Valdecir Janasi[2]; Renato Henrique-Pinto[2]; Adriana Alves[2]; Natasha Sarde Marteleto[2]

[1]Sciences de la Terre, Université du Québec à Chicoutimi, Québec, G7H 2B1, Canada

[2]Instituto de Geociências, Universidade de São Paulo, Brazil

https://doi.org/10.1016/j.lithos.2021.106374 **Abstract**

The concentrations of Te, As, Bi, Sb and Se (TABS+) in magmas from large igneous provinces (LIPs) are of interest because these elements are important in the formation of platinum-group minerals (PGM) found in magmatic Ni-Cu platinum-group element (PGE) deposits. Furthermore, the TABS+ are volatile and hence they may be lost in degassing and have a role to play in the mass extinctions associated with LIPs events because these are mostly toxic elements. However, the concentrations of TABS+ in magmas from LIPs are not well documented due in part to the analytical difficulties and in part to the numerous processes that affect their distribution. We have determined the concentration of TABS+ and PGE in rocks from the Paraná Magmatic Province (PMP) in order to assess the effects of fractional crystallization, sulfide segregation and magma degassing. Decrease in the Rh, Ru and Ir concentrations with Mg and Cr indicate that these elements behaved as compatible elements during crystal fractionation. Based on changes in the Cu/Pd sulfide saturation occurred in some cases resulting into a decrease in Pd and Pt. Arsenic and Sb behave as incompatible elements, whereas Se, Te and Bi show variable behavior. Most lavas from the PMP display negative As, Se and Te anomalies on mantle-normalized patters coupled with Te/Cu, Se/Cu and As/Th and Sb/Th

ratios lower than mantle values, which we attribute to loss of the TABS+ during degassing.

Key words: Paraná Magmatic Province; Te, As, Bi, Sb and Se (TABS+); Platinum-group element; Fractionation; Sulfide segregation; Degassing

*Corresponding author: etmansur@gmail.com

1 – Introduction

The distribution of chalcophile elements such as the platinum-group elements (PGE) in lavas from different geological settings has been extensively investigated over the past decades (Barnes et al., 1985; Bockrath et al., 2004; Pitcher et al., 2009; Hughes et al., 2015). However, recent contributions have also investigated a wider range of chalcophile elements, which include Te, As, Bi, Sb (TABS) and Se (Jenner and O'Neill, 2012; König et al., 2012; Lissner et al., 2014; Mansur et al., 2020a; Maciag and Brenan, 2020). The interest in better understanding the distribution of PGE and TABS in rocks from different environments is the result of their ability to record a wide range of geological processes. These processes include Earth's differentiation, fractional crystallization, crustal assimilation, sulfide segregation, magma degassing (König et al., 2012; Lissner et al., 2014; Edmonds et al., 2018; Wieser et al., 2020; Maciag and Brenan, 2020), and the formation of mineral deposits (Chen et al., 2013; Mansur and Barnes, 2020a, Mansur et al., 2020a).

In the current work we present new whole-rock analyses of S and PGE, and the first TABS and Se (TABS)+ analyses for samples from different portions of the Paraná Magmatic Province (PMP). The rocks represent both high- and low-Ti basalts (summarized by Peate 1997) and intrusive rocks from the Ponta Grossa and

Florianópolis dyke swarms. The results are presented together with those for samples with previously published PGE results from the PMP (Mincato, 2000; Rocha-Júnior et al., 2012), and also from the Etendeka Province (Maier et al., 2003; Barnes and Mansur, *in press*), which together form a Large Igneous Province (LIP) – the Paraná-Etendeka Magmatic Province (PEMP). Results for TABS+ are also compared with previously obtained values for other LIPs to refine our understanding of their geochemical cycle. This contribution documents the effects of fractional crystallization, sulfide segregation and magma degassing on the distribution of PGE and TABS+ in the PMP.

2 – Regional Setting

The PEMP is a LIP associated with the Gondwana break-up during Early Cretaceous (~135-130 Ma) and the opening of the South Atlantic Ocean (Peate, 1997; Thiede and Vasconcelos, 2010; Janasi et al., 2011; Pinto et al., 2011a). It comprises mainly subaerial lavas and related dyke swarms at central South America (Brazil, Argentina, Uruguay, and Paraguay) and southwestern Africa (Angola and Namibia). In total, the PEMP covers an area of approximately 920,000 km^2 (Frank et al., 2009), of which the vast majority is exposed in the Paraná Sedimentary Basin, South America (Fig. 1). The remaining African counterpart of the province comprises the bimodal magmatism exposed in the Etendeka region (Maier et al., 2003; Frank et al., 2009; Marsh and Swart, 2018).

In Brazil, the volcanic pile is referred to as the Serra Geral Group (Fodor et al., 1989; Rosseti et al., 2018), and reaches up to 1700 m thick in the central portion of the basin (Frank et al., 2009). The rocks are divided on the basis of geochemical criteria, comprising six basaltic and two silicic magma types. The basaltic magma types are

divided into the northern high-Ti Pitanga, Paranapanema and Ribeira, the southern low-Ti Gramado and Esmeralda, and the north-eastern high-Ti-Sr Urubici. Similarly, the silicic magmas are divided into the high-Ti Chapecó, and the low-Ti Palmas (Mantovani et al. 1985; Peate et al., 1992; Guimarães et al., 2019). Recent advances on the understanding of the stratigraphy of the Paraná lavas have allowed for refining these classifications (Polo et al., 2018; Rosseti et al., 2018). For instance, Rosseti et al. (2018) proposed the division of the low-Ti Gramado and Esmeralda magma types, from the base to top, into the Torres, Vale do Sol and Esmeralda Formations. Moreover, it is also possible that the Esmeralda Formation is equivalent to the Barros Cassal sequence, defined by Polo et al. (2018) as an andesitic basalt to dacite sequence emplaced between the Vale do Sol Formation and the upper low-Ti silicic units of rhyolitic composition.

Three main basaltic dyke swarms occur along the coastal areas of Brazil and represent, at least partly, the plumbing systems that fed the magmas from the PEMP (Florisbal et al., 2014). These dyke swarms coeval to the Paraná lava flows (Janasi et al., 2011; Pinto et al., 2011a; Florisbal et al., 2014; Almeida et al., 2018) also show the continuity of radiating structures in the African continent, allowing the genetic link with the Etendeka margin counterparts (Marsh and Swart, 2018; Beccaluva et al., 2020). From north to south the dyke swarms are the NE-SW Santos-Rio de Janeiro, the NW-SE Ponta Grossa, and the nearly N-S Florianópolis (Fig. 1). The Ponta Grossa dyke swarm is dominated by high-Ti basalts compositionally similar to the Pitanga and Paranapanema magma types (Peate et al., 1992; Almeida et al., 2018). The Florianópolis dyke swarm comprises high-Ti-Sr basalts similar to the Urubici magma type (Florisbal et al., 2014). The Santos-Rio de Janeiro dyke swarm is relatively more

complex and younger, comprising rocks with alkaline and tholeitic affinities (Bennio et al., 2003).

3 – Sample selection and dataset

The set of samples selected for analyses of PGE and TABS+ in this work thought to be representative of the main varieties of basalts present in the PMP and was based on work now under development. We selected 39 samples representative of the different basaltic magma types from the Serra Geral Group and correlated dyke swarms, which from now on we refer as the Paraná Magmatic Province (PMP; Fig. 1). These comprise 8 samples from the high-Ti flows of the northern portion, 12 samples from the low-Ti flows of the southern portion, 14 samples from the Ponta Grossa dyke swarm, and 5 samples from the Florianópolis dyke swarm. All the samples from the northern high-Ti flows represent the Pitanga magma type, whereas samples from the southern low-Ti flows include the Vale do Sol Fm. (n=3), Torres Fm. (n=3), Esmeralda Fm. (n=2) and Barros Cassal sequence (n=4). Samples from the Ponta Grossa dyke swarm (sills, dykes and their corresponding volcanic flows) have geochemical affinities with Pitanga (n= 8) and Paranapanema (n= 6) magma types, whereas those from the Florianópolis dyke swarm present affinities with the Urubici type.

The PGE analyses of Rocha-Júnior et al. (2012), obtained using isotopic dilution and allowing for very low detection limits, for the Esmeralda (n= 6), Paranapanema (n= 3), Pitanga (n= 1) and Urubici (n=1) magma types, and the results from Mincato (2000) which are not available in the English literature for the Gramado (n= 16), Pitanga (n= 4), Paranapanema (n= 3) and Urubici (n= 2) types are included for comparison. Results for PGE from Maier et al. (2003) and TABS+ from Barnes and Mansur (*in press*) for the Horingbaai (n= 3) and Tafelberg (n= 3) members of the

Etendeka Province are also included. Other contributions have also investigated the distribution of PGE (or at least some of them) in rocks from the PMP (Romanini and de Albuquerque, 2001; Crockett, 2002; Pinto et al., 2011b; Arena et al., 2014). Although some of these contributions did not focus specifically on the controls on the distribution of PGE, we have also compared their results with our values in order to check for major discrepancies.

4 – Analytical methods

The analyses of whole rocks by X-ray fluorescence and ICP-MS listed in Electronic Supplementary Material (ESM, Table 1) were kindly provided by colleagues, whose names are indicated in ESM (Table 1) and are part of datasets from manuscripts in preparation.

Tellurium, As, Bi, Sb and Se analyses were carried out by Hydride Generation-Atomic Fluorescence Spectrometry (HG-AFS) following the technique described by Mansur et al. (2020b), at LabMaTer, Université du Québec à Chicoutimi (UQAC). International reference materials (CH-4 and TDB-1 from Natural Resources Canada; OKUM from IAGEO), and a blank were determined at the same time as the samples, and the results agree with working values (ESM, Table 2). The 3σ detection limits are 0.006, 0.003, 0.007, 0.009 and 0.003 ppm for Te, As, Bi, Sb and Se, respectively.

Platinum-group elements (Os, Ir, Ru, Rh, Pd, and Pt) and S were also analyzed at LabMaTer, UQAC. The PGE were pre-concentrated by Ni-sulfide fire assay and co-precipitated with Te, and analyzed by solution inductively coupled plasma – mass spectrometry (ICP-MS) using the method described by Savard et al. (2010). Sulfur was determined by combustion and infrared analysis using a HORIBA EMIA-220V

155 analyser using the method described by Bédard et al. (2008). International reference
156 materials (OKUM and GeoPT-18/KPT-1, from IAGEO; LK-NIP-1 and LDI-1, from
157 Geo Labs - OGS) were analyzed with the samples to monitor data quality. The results
158 obtained for the reference materials are consistent with the working values (ESM,
159 Table 3).

160 Whole-rock major oxides and some trace-elements were analyzed by X-ray
161 Fluorescence at the Geonalitica Core Center, Instituto de Geociências, Universidade
162 de São Paulo, Brazil, following the protocol described in Mori et al. (1999). Analyses
163 were performed in a Panalytical AXIOS MAX Advanced spectrometer. Major and
164 minor elements were analyzed from molten tablets obtained from 1g sample and 9g of
165 a mixture of spectroscopic grade lithium tetra and metaborate at 1100-1200^{o} C in a
166 platinum crucible, using a Claisse fusion machine. Trace elements were analyzed from
167 pressed pellets obtained from homogenization of the pulverized sample (previously
168 micronized in a McCrone Micronizer) with wax. Analytical quality was controlled
169 using reference materials JB-1a and JG-1a as unknown samples, and duplicate samples
170 (ESM, Table 4).

171 Rare earth and other trace elements were determined by ICPMS at the
172 Geonalitica Core Center, Instituto de Geociências, Universidade de São Paulo, Brazil,
173 following the protocol described in Navarro et al (2008). Analyses were performed in
174 a Thermo-Analitica iCAP quadrupode analyzer. Powdered samples were dissolved by
175 acid attack with concentrated HF and HNO_3 in microwave oven (aphanitic and fine-
176 grained volcanic rocks) or in Parr bombs (medium-grained intrusive rocks). Analytical
177 quality control was checked by the analyses of reference materials JG-1a and JR-1 as
178 unknown samples, blank and duplicate samples (ESM, Table 4).

5 – Results

5.1 – Fractionation of the magmas

The rocks from the PMP are classified as high-Ti and low-Ti magma series (Mantovani et al. 1985; Peate et al., 1992; Guimarães et al., 2019). Samples from the high-Ti series have Ti concentrations greater than 10,000 ppm and Ti/Y ratios above 350, whereas most low-Ti rocks have Ti contents lower than 10,000 ppm and Ti/Y ratios ranging from 200 to 400 (Fig. 2a and 2b). Moreover, high-Ti rocks have higher La/Yb and Sm/Yb ratios, ranging from 7 to 13 and 2 to 4, respectively, than low-Ti rocks in which these range from 2 to 10 and 1 to 2.5, respectively (Fig. 2c and 2d). The Urubici type magmas have similar Ti contents and Ti/Y ratios to high-Ti rocks, but even higher La/Yb and Sm/Yb ratios, ranging from 15 to 18 and 3.8 to 4.5, respectively (Fig 2).

The distribution of Mg# (i.e. ([Mg]/[Mg+Fe] x 100)) and other major and minor elements (Al_2O_3, Fe_2O_3, CaO, Ni, Cr and Cu) are shown in Fig. 3. Samples from the high-Ti and Urubici varieties have lower Mg# relative to low-Ti magma type, whereas the highest Mg# are found in picrites from the Etendeka Province (Fig. 3). There is a positive correlation between Al_2O_3, CaO, Ni and Cr with Mg#, and a negative correlation between Fe_2O_{3T} and Cu with Mg# (Fig. 3). These variations suggest progressive crystallization of clinopyroxene and plagioclase during fractionation of these liquids. Also, the increase in Al_2O_3 and CaO and decrease in Fe_2O_3 from Etendeka picrites into the more primitive magma composition (i.e. higher Mg#) from the PMP support the early olivine removal from these liquids. The decrease in Cr values with progressive fractionation may reflect the crystallization of accessory chromite, especially from more primitive magmas. The Cu values increase with

decreasing Mg#, thus reflecting its incompatible behaviour during silicate crystallization. However, there are a few samples at Mg# close to 35 that display Cu depletion, thus supporting that fractional crystallization was at least partially accompanied by sulfide removal.

The results for PGE are broadly in agreement with previously published values (Mincato, 2000; Crockett, 2002; Romanini and de Albuquerque, 2001; Pinto et al., 2011b; Rocha-Júnior et al., 2012; Arena et al., 2014). Given that no major discrepancies were found between our results and literature values, and that we do not aim to provide a review of PGE results within PMP, we acknowledge previous studies but only include the data from Mincato (2000) and Rocha-Júnior et al. (2012) in our plots. These contributions provide representative examples from literature values and cover a similar sampling extension to our samples. Platinum and Pd concentrations vary from 3 to 20 ppb and although scattered, there is a slightly increase in concentrations following fractional crystallization (Fig. 4a and 4b). The exceptions are a few high-Ti rocks from the Pitanga magma type located at the northern portion of the PMP, which have Pt and Pd concentrations below 1 ppb, most likely reflecting the effect of sulfide removal. Rhodium and Ru concentrations are mostly below 0.7 and 0.3 ppb, respectively, and decrease during fractional crystallization (Fig. 4c and 4d). Many of our samples have Ir, and especially Os, concentrations below their detection limits, and most samples with detectable amounts have less than 0.5 and 0.2 ppb, respectively (Fig. 4e and 4f). The exceptions are picrites from the Etendeka Province, which have Ir and Os concentrations ranging from 0.5 to 2 ppb. Thus, Ir and Os concentrations decrease following progressively fractional crystallization (Fig. 4e and 4f).

Concentrations of Se, Te and Bi do not correlate with Mg# (Fig. 5). Selenium and Te concentrations fall mainly below 0.1 and 0.01 ppm, respectively, with the exception of dykes from the Ponta Grossa dyke swarm and the Etendeka Province, which have slightly greater contents (Fig. 5a and 5b). Bismuth concentrations are more widespread, and although concentrations in samples from the Ponta Grossa dyke swarm are also among the highest values, there is a vast overlap with other samples (Fig. 5c). It is noteworthy that Se, Te and Bi concentrations found in some samples from the PMP, especially from the Ponta Grossa dyke swarm, are among the highest values compared to other LIP (Fig. 5a to 5c), which could be related to the more fractionated character of rocks from the PMP. In contrast to other TABS+, As and especially Sb, show an incompatible behaviour, and concentrations increase following progressively lower Mg#. Arsenic concentrations vary mainly from 0.05 to 0.5 ppm, whereas Sb values vary from 0.03 to 0.2 ppm (Fig. 5d and 5e). The increase in Sb concentrations is also followed by other incompatible elements (e.g. Nb in Fig. 5f), which support its incompatible behaviour during fractional crystallization.

5.2 – The PGE distribution

Samples from both high-and low-Ti types from the PMP display highly fractionated mantle-normalized PGE patterns, with strong IPGE (Ir, Os and Ru) and Rh depletion relative to Pt and Pd (Fig. 6). A few high-Ti samples are also depleted in Pt and Pd relative to Cu (Fig. 6a), and this feature is also observed in the data from Mincato (2000). Slightly negative Ru anomalies are observed in few mantle-normalized patterns from both high- and low-Ti rocks. There is no major variation in mantle-normalized patterns from different formations within low-Ti rocks (Fig. 6b). In contrast, the Ponta Grossa dyke swarm patterns for the Paranapanema type magmas are slightly enriched relative to those for the Pitanga type magmas (Fig. 6c). Samples

from the Florianópolis dyke swarm also display IPGE-depleted patterns, but no clear negative Ru anomalies (Fig. 6d).

Platinum and Pd show a broad positive correlation, but the Pt/Pd ratios are variable within the PMP (Fig. 7a). The Pt/Pd ratios of our dataset vary from 0.5 to 2 with no clear distinction between high-Ti and low-Ti rocks. A clear distinction, however, is observed among the high-Ti basalts, with our Paranapanema samples showing lower Pt/Pd (mostly <1), which reflect high Pd contents (>10 ppb), whereas Pitanga spreads over a roughly trend at higher (1.5-2) Pt/Pd. High Pd contents are also shown by the Paranapanema samples analysed by Mincato (2000), that have Pt/Pd ratios even lower than ours, but not by the Paranapanema flows analysed by Rocha-Júnior et al. (2012) (Fig. 7a). Therefore, it is not possible to clearly separate high-Ti and low-Ti rocks based only on their Pt/Pd ratios. Palladium also shows a moderate positive correlation with Rh (Fig. 7b), but no correlation with Ir. Palladium/Ir ratios vary widely within the PMP, ranging from ~ 25 to 300 in both low-Ti and high-Ti rock types, however, for most of the samples the ratio varies from 50 to 200 (Fig. 7c). Rhodium shows no clear correlation with IPGE (Fig. 7d), whereas Ru and Os display a positive correlation (Fig. 7e). Iridium and Os show no correlation but is noteworthy that concentrations of both elements are close to their detection limits (Fig. 7f).

5.3 – The TABS+ distribution

The distribution of TABS+ can be readily assessed using the mantle-normalized diagram (Fig. 8), proposed by Barnes and Mansur (*in press*). The use of the diagram is detailed by the authors and only a summary is provided here. In order to assess the effect of sulfide liquid segregation, or sulfide liquid accumulation, the elements are arranged in

order of partition coefficient into a sulfide liquid (Liu and Brenan, 2015). To take into consideration the effects of degree of partial melting and/or crystal fractionation Th, Nb were added to the diagram as representatives of the lithophile incompatible elements. The TABS+ and S are volatile (Lodders, 2003), and therefore subaerial lavas could be depleted in these elements during degassing. In order to take this into consideration, chalcophile elements that are less volatile (Cu, Pd, and Pt) were added to the plot at the position of their relative partition coefficients into base metal sulfide liquid.

Most of the samples show similar patterns with overall negative slopes decreasing from Th and Nb mantle-normalized values in the 50 to 200 range to Pd and Pt values in the 1 to 3 range. A few high-Ti Pitanga magma type are the exceptions and are more strongly depleted in Pt and Pd (Fig. 8a). Most samples also show negative As, Se and Te anomalies. In samples from the Ponta Grossa dyke swarm these negative anomalies are variable and tend to be more pronounced in volcanic rocks relative to the subvolcanic ones (Fig. 8c). The patterns for samples from different localities do, however, show differences in Th to Nb ratios. Most of the high-Ti rocks are not enriched in Th (Fig. 8a, 8c and 8d), whereas low-Ti types are enriched in Th (Figs. 8b), and this Th enrichment is best explained by crustal assimilation (Peate and Hawkesworth, 1996). Few low-Ti and most Urubici type lavas display slightly positive Bi anomalies (Fig. 8b and 8d).

6 – Discussion

6.1 - The effect of chromite and olivine crystallization

The behaviour of PGE during the fractionation of mafic rocks has been extensively considered in different geological contexts worldwide (Barnes et al., 1985; Maier et al., 2003; Bockrath et al., 2004; Pitcher et al., 2009; Hughes et al., 2015).

More primitive lavas display relatively flat mantle-normalized PGE patterns. In contrast, progressively more fractionated lavas show an IPGE (Ru, Ir and Os) depletion relative to PPGE (Pt, Pd and Rh), and the PPGE/IPGE ratios tend to increase antithetically to Mg# (Barnes et al., 1985; Day et al., 2013; Arguin et al., 2016). Although sulfide saturation would be expected during fractional crystallization, sulfide removal is not thought to be responsible for fractionating PPGE from IPGE, as both have similar partition coefficients into the sulfide liquid (Mungall and Brenan, 2014; Liu and Brenan, 2015). Thus, alternative processes must take place to explain the preferential IPGE removal during fractional crystallization.

Some authors have highlighted the potential association of PGE-alloys (mainly IPGE-alloys) and chromite grains in volcanic rocks (Locmelis et al., 2011; Arguin et al., 2016). Indeed, experimental studies support crystallization of some PGE in the boundary layer of chromite (Finnigan et al., 2008). Moreover, several authors also demonstrate the preferential partition of IPGE not only into chromite, but also into olivine (Righter et al., 2004; Pagé et al., 2012; Arguin et al., 2016; Park et al., 2017). Therefore, the early olivine and chromite removal from primitive magmas could explain the IPGE-depleted patterns observed in more fractionated rocks. For instance, the rocks from the PMP fall in the lowermost depleted end of a positive correlated trend observed between Cr and IPGE for magmas from different LIPs (represented by Ir in Fig. 9a). This suggests that chromite removal during early fractional crystallization may be as least partially accountable for the IPGE depletion observed in the PMP rocks.

In contrast to other LIPs, there is a lack of the more primitive end members in the continental flood basalts from the PMP. Although picrites are observed in the Etendeka Province (Thompson et al., 2001; Maier et al., 2003; Jennings et al., 2019),

these primitive rocks are not found in the South American counterpart of the province (Peate et al., 1992; Rosseti et al., 2018; Beccaluva et al., 2020). However, modelling results reveal that the early olivine crystallization, and probably chromite, have occurred during fractionation of the PMP magmas (Jennings et al., 2019; Beccaluva et al., 2020). Therefore, it is likely that the IPGE depletion observed in the PMP magmas reflects the formation of IPGE-alloys in response to chromite crystallization, or also the partition of Rh and IPGE into chromite and olivine lattice upon early fractionation. Thus, the progressive fractionation would lead to progressively lower Rh and IPGE concentrations (Fig. 9a), but would not decrease Pt and Pd, leading to progressively higher Pd/Ir ratios (Fig. 9b). Also, higher Rh and IPGE values, accompanied by higher Cr contents in picrites from the Etendeka Province (e.g. Ir in Fig. 9a), and lower Pd/Ir ratios (Fig. 9b), provide additional support for the role of chromite in removing IPGE during fractional crystallization.

The shapes of mantle-normalized PGE patterns also argue for IPGE removal in response to chromite crystallization. Arguin et al. (2016) estimated the partition coefficients for Rh and IPGE between chromite/melt and demonstrated that Ru has a higher partition coefficient into chromite relative to Rh, Ir and Os. The authors then argue that chromite crystallization would lead to a more pronounced depletion of Ru relative to Rh, Ir and Os in the melt. This would be recorded by negative Ru anomalies in mantle-normalized PGE patterns from more fractionated magma compositions (Park et al., 2017). Our results support this interpretation, as some of the IPGE-depleted mantle-normalized patterns display negative Ru anomalies (Fig. 6). Therefore, we argue that the decoupling of PPGE and IPGE in the rocks from the PMP was likely caused by the crystallization of chromite, and olivine, during early fractionation of the PMP magma types. This interpretation is also complimentary to

the conclusions drawn by Day et al. (2013). The authors argued that fractionated mantle-nomalized PGE patterns like those found at the PMP were caused by the crystallization of IPGE-bearing alloys during magma fractionation.

6.2 -The effect of sulfide segregation

Given the chalcophile nature of TABS+ and PGE, sulfide segregation or accumulation are among the most important processes affecting their distribution (Patten et al., 2013; Mungall and Brenan, 2014; Liu and Brenan, 2015; Mansur et al., 2020b). Although S contents are below detection limits for most samples, there is a positive correlation between S and Se for samples with contents above detection limits. These samples are mainly from dykes and sills of the Ponta Grossa and Florianópolis dyke swarms, and also dykes from the Etendeka Province (Fig. 10a). For these samples, S/Se ratios vary from 1200 to 3400 (one sample yields 4600), which are close to or below mantle values (i.e. approximately 3050; Lyubetskaya and Korenaga, 2007). Sulfur/Se ratios greater than mantle values are argued to result from S assimilation from country rocks, whereas ratios lower than mantle values are indicative of S loss (Queffurus and Barnes, 2015 and references therein). In the case of the PMP, the fact that higher concentrations are found in subvolcanic rocks suggests loss by degassing upon eruption, which display no detectable contents of both S and Se. The effect of magma degassing on the distribution of chalcophile elements will be considered in the next section below. Because the precision of the Se analyses (Mansur et al., 2020b) is higher than of S analyses (Bédard et al., 2008), Se is used as a proxy for S.

There is a broad positive correlation between Pd and Se for most samples, apart from the high-Ti flows of Pitanga type (Fig. 10). Also, the Se and Pd concentration

ranges for samples from the PMP are similar to those observed in other LIPs. There is also a broad positive correlation between Te and Bi and Se for the dyke samples from the Ponta Grossa dyke swarm. The positive correlation between Pd, Te, Bi and Se is in agreement with these elements being moderately to highly chalcophile, and thus their distribution being controlled by the presence of sulfide minerals (Mansur and Barnes, 2020a, 2020b). In contrast, As and Sb concentrations vary regardless of Se contents, which is also in agreement with these elements being only slightly chalcophile, and their distribution not being significantly affected by the presence of sulfide minerals (Maciag and Brenan, 2020; Mansur and Barnes, 2020b). Also of note is that the As and Sb concentrations in samples from the PMP are amongst the lowest values found in other LIP. The concentrations of these elements in mafic magmas are normally upgraded in response to crustal assimilation (Barnes and Mansur, *in press*), which is counterintuitive given that crustal assimilation is supported by mantle-normalized patterns for at least part of the rocks from the PMP (Fig. 8). One possibility is that the contaminants at the PMP were not particularly enriched in As and Sb, but further investigations on this topic are still necessary prior to more conclusive interpretations.

Variations in Cu and PGE contents in some of the PMP rocks suggest that sulfide segregation occurred during the fractionation of the magmas (Fig. 3f and 4). A possible manner of tracking sulfide removal is by investigating Cu/Pd ratios in different samples (Barnes et al., 1993; Maier et al., 1996). Both Cu and Pd are considered incompatible elements during fractional crystallization in the absence of a sulfide liquid, but once an immiscible sulfide liquid segregates both elements are sequestered from the silicate magma. However, the partition coefficients between sulfide and silicate liquid are higher for Pd than for Cu (Barnes et al., 1993; Maier et

409 al., 1996). Therefore, the depletion of Pd relative to Cu can be used as a tool for
410 estimating the degree of fractional crystallization under sulfide-saturated conditions
411 that a given magma underwent.

412 Figure 11 shows a binary plot of Cu/Pd versus Pd for the studied samples. We
413 have calculated a curve representing the crystallization under sulfide-saturated
414 conditions in cotectic proportions to estimate the amount of sulfide removal for
415 different samples. The used partition coefficients for Pd and Cu between silicate and
416 sulfide liquids were of 400,000 and 1,500, respectively (Mungall and Brenan, 2014).
417 The concentrations of both elements in the fractionated liquid ($\mathbf{C}_f$) was calculated
418 using to the following equation:

419 Rayleigh fractionation:

420 $$\mathbf{C}_f = \mathbf{C}_i \mathbf{F}^{[(\mathbf{D}sul\mathbf{F}sul)-1]}$$

421 where $\mathbf{C}_i$ is the concentration of the element in the initial liquid, **F** is the weight fraction
422 of remaining liquid, $\mathbf{D}_{Sul}$ is the partition coefficient of the element between silicate and
423 sulfide liquids, and $\mathbf{F}_{Sul}$ is the weight fraction of sulfide liquid in cotectic proportions.
424 We assumed the S content at sulfide saturation at about 1,500 ppm (Li and Ripley,
425 2005). This value and the average S content in magmatic sulfides (approximately 35
426 wt. %) were used to estimate the weight fraction of sulfide liquid in cotectic
427 proportions (approximately 0.004). Concentrations of Pd and Cu in the transporting
428 melt at sulfide saturation were assumed at 15 ppb and 160 ppm, respectively.

429 Most samples from the PMP show evidence for sulfide removal with Cu/Pd
430 ratios higher and Pd values lower than initial liquids, and mantle-derived magmas (Fig.
431 11). The Cu/Pd ratios and Pd values observed for most samples can be modelled by up

to 0.5% crystallization under with sulfide segregation in co-tectic proportions. Four high-Ti samples do require a slightly more extensive sulfide removal, and approximately 2.5% bulk crystallization under sulfide-saturated conditions in order to reproduce their Cu/Pd and Pd values. This understanding is critical for exploration programs given that PGE- and base metal-depleted volcanic rocks are associated to large magmatic sulfide deposits in other LIP (Lightfoot et al., 1994; Jowitt and Ernst, 2013). Thus, our results support the sulfide removal at cotectic proportions during the fractionation of most the PMP magma types, but only locally more extensive sulfide removal has occurred. In fact, this was observed specifically in the Pitanga type high-Ti magma compositions.

Another observation that is possibly explained by the sulfide removal from rocks of the PMP is the negative slope found in mantle-normalized Th, Nb, Cu, TABS+, Pt, Pd spidergrams (Fig. 8). In these plots, the elements are organized from left to right following progressively higher partition coefficients into an immiscible sulfide liquid, following Barnes and Mansur (*in press*). Therefore, given the cotectic sulfide removal from PMP, the negative slopes of the patterns probably reflect the preferential removal of highly chalcophile elements relative to slightly chalcophile ones. However, although the negative slopes may be explained by sulfide removal, As, Se and Te negative anomalies cannot be explained by different partition coefficients of these elements into an immiscible sulfide liquid. For instance, Se and Te have lower partition coefficients into a sulfide liquid than both Pt and Pd, thus their negative anomalies cannot be explained by sulfide removal. Therefore, some additional process is needed to explain these recurrent negative anomalies found in rocks from the PMP.

6.3 -The effect of low-pressure degassing upon eruption

Understanding the distribution of volatile elements in subaerial lavas is not straightforward given that degassing under lower pressure eruption may diminish their original concentrations. Because TABS+ have relatively low condensation temperatures during the formation of the solar system they are classified as volatile elements (Lodders, 2003). Moreover, the presence of TABS+, together with S, in volcanic gases is also supportive of their loss upon eruption (Self et al., 2005; Zelenski et al., 2014; Forrest et al., 2017; Wieser et al., 2020). The presence of negative As, Se and Te anomalies in mantle-normalized patters could result from the loss of these elements upon degassing. The size of the anomalies based on neighbour elements in mantle-normalized plots suggests that more than 80% of these elements were potentially lost (relative difference from dashed black line in figure 8). An interesting observation is that subvolcanic rocks from the Ponta Grossa dyke swarm show less pronounced negative anomalies, which is suggestive that degassing was less intense in these rocks.

Barnes and Mansur (*in press*) have compared the distribution of TABS+ in subaerial rocks from different LIPs and in subaqueous rocks, such as MORB. Similar negative As, Se and Te anomalies were observed in mantle-normalized plots for rocks from various LIPs but were not present in MORB. The authors used TABS+/Cu ratios to estimate the effect of degassing because Cu is less volatile than TABS+, and thus lower ratios are suggestive of degassing. This assumption is supported by the presence of native Cu in some subaerial lavas argued to have experienced S loss (Harris, 1987; Arguin et al., 2016; Li and Boudreau, 2017). Moreover, previous studies also highlight the presence of native cooper in rocks from the PMP, thus supporting a similar process (Pinto et al., 2011b; Baggio et al., 2018).

The Se/Cu and Te/Cu ratios in the PMP samples are mostly lower than mantle values (Fig. 12a and 12b), which supports that Se and Te have been lost by degassing. Also, the values are in the same range of those found at other subaerial lavas from different LIP. It is also noteworthy that Se/Cu ratios in these samples are significantly lower than those found in MORB, for which degassing is diminished by greater eruption depths (Mathez, 1976; Lissner et al., 2014). Tellurium/Cu ratios in MORB are also lower than mantle values, but this does not necessarily reflect Te loss by degassing (Fig. 12b). Tellurium has a greater partition coefficient into sulfide liquid than Cu (Patten et al., 2013; Liu and Brenan, 2015), and therefore sulfide removal could lead to lower Te/Cu ratios. In the case of the PMP, however, sulfide removal would not account for lower Te/Cu ratios in most samples because Te/Pd ratios are lower than mantle. Given that Te has a lower partition coefficient into the sulfide liquid relative to Pd, sulfide removal should yield Te/Pd ratios greater than mantle values. Therefore, Te/Cu ratios lower than mantle in the PMP rocks support Te loss upon degassing.

The Bi/Cu ratios show a wide range, but most values for the PMP are close to, or slightly greater than mantle values (Fig. 12c). Barnes and Mansur (*in press*) also report a wide variation in Bi/Cu ratios in various LIP. The authors argue that Bi distribution reflects the overprinted effect of crustal assimilation, sulfide removal or accumulation and potentially loss by degassing. Consequently, Bi/Cu ratios may not directly record the effect of degassing. High- and low-Ti rock varieties show different degrees of crustal assimilation (Peate et al., 1992; Rocha-Júnior et al., 2013; Rosseti et al., 2018; Beccaluva et al., 2020), however similar Bi/Cu ratios suggest no major influence from these processes in Bi concentrations at the PMP. The reasons for the

scattering in Bi/Cu ratios observed at the PMP, and also other LIPs, are not fully understood at this time.

Because As and Sb are only slightly chalcophile elements and show an incompatible behaviour, we used As/Th and Sb/Th ratios to consider the effect of degassing on these elements. Moreover, Barnes and Mansur (*in press*) demonstrated that As and Sb concentrations, and Th, may be variably upgraded by assimilation of crustal material. Thus, lower ratios could reflect As and Sb loss by degassing, whereas higher ratios could reflect the assimilation of different crustal components (e.g. average upper crust, black shale). Samples from the PMP have As/Th and Sb/Th ratios lower than mantle values (Fig. 12d and 12e). These values are lower than most results found at other LIP, for which As/Th and Sb/Th ratios are mainly close to mantle values. However, at other LIPs the values close to mantle are interpreted to reflect the combined effect of As and Sb upgrading by crustal assimilation (Barnes and Mansur, *in press*) and fractional crystallization (Maciag and Brenan, 2020), and their loss upon degassing. An upgrade of As and Sb due to crustal assimilation in samples from the PMP is not supported by our results. For instance, low-Ti volcanoc rocks have positive Th mantle-normalized anomalies (Fig. 8b), supporting crustal assimilation, but no upgrade in As or Sb concentrations. Thus, in the case of the PMP, ratios lower than mantle values suggest As and Sb loss upon degassing.

6.4 – Potential relationship between LIPs emplacement and mass extinctions

Understanding the input of volatile elements into the atmosphere caused by the emplacement of LIPs is a long-debated issue. One of the main motivations for these studies is to assess either the volatile input may contribute to mass extinctions, which were frequently coeval to the formation of various LIPs (e.g. Wingall, 2001).

However, although the association of LIP emplacement and mass extinction events is common, no such correlation has been documented for the PMP yet. For instance, Callegaro et al. (2014) argued that lower magmatic S contents in the PMP magmas could explain the lower environmental impact relative to other LIPs associate to mass extinctions (Wignall, 2001; Callegaro et al., 2014; Heimdal et al., 2019). Therefore, understanding how the environmental impacts caused by the emplacement of the PMP differ from those caused by the emplacement of other LIPs is critical to better understand the link between LIPs and mass extinctions.

Our results do support the loss of S, Te, Se, As and Sb during the emplacement of the PMP. These have been considered as toxic elements, and their upgrade in the atmosphere may have an environmental impact (e.g. Vandenbroucke et al., 2015). However, quantifying the amount of these elements released in the atmosphere is not straightforward as initial concentrations are not readily assessed. Also, an additional problem is that metal input during LIP emplacement may also derive from heating and degassing of the host rocks (Ganino and Arndt, 2009; Heimdal et al., 2019), and not only from magma degassing. One possibility for assessing initial concentrations of TABS+ in volcanic rocks from different LIPs would be by investigating their concentrations in melt inclusions (Wallace and Edmonds, 2011). We suggest that future contributions in this domain would further help refining our understanding on the link between magma degassing upon LIP emplacement and mass extinctions.

7 – Conclusions

We investigated the distribution of PGE and TABS+ in volcanic and subvolcanic rocks from the Paraná Magmatic Province (PMP). Our main findings are summarized as follows:

1 – Distributions of PGE and TABS+ in the PMP rocks allows assessing the effects of fractional crystallization, sulfide segregation and magma degassing.

2 - Crystallization of olivine and chromite at early stages of magma fractionation led to a depletion of Rh and IPGE in samples from the PMP. The effect of chromite removal is also recorded by negative Ru anomalies in mantle-normalized PGE patterns. Platinum and Pd are not affected by olivine and chromite crystallization, and show an incompatible behaviour, thus becoming more concentrated during progressive fractionation.

3 – Selenium, Te and Bi do not record the effect of fractional crystallization as their distribution is overprinted by other processes. On the other hand, As and Sb are incompatible, and their concentrations increase in progressively more fractionated rocks.

4 – Most magma varieties from the PMP rocks display Cu/Pd ratios higher and Pd contents lower than mantle values, which support up to 0.5% bulk crystallization under sulfide-saturated conditions. However, a few high-Ti samples do require around 2.5% crystallization under sulfide-saturated conditions to reproduce their Cu/Pd ratios and Pd contents.

5 – Most lavas from the PMP display negative As, Se and Te anomalies on mantle-normalized patters, which coupled with Te/Cu, Se/Cu and As/Th and Sb/Th ratios lower than mantle values, support their loss upon degassing. The effects of magma degassing for these elements is less pronounced in subvolcanic rocks from the Ponta Grossa and Florianópolis dyke swarms relative to subaerial lava flows.

Acknowledgements

This work was supported by a Canada Research Chair program grant to Sarah-Jane Barnes (215503) and Discovery Grant 1884-2013. Valdecir Janasi acknowledges the

Fapesp Thematic Projects 2012/06082-6 and 2019/22084-8 for the support. This manuscript benefited from insightful comments from the reviewers Lie-Meng Chen and David Peate and careful editorial handling by the editor Greg Shellnutt.

Figure Captions

Figure 1 – Simplified geological map illustrating the distribution of the main lavas in the Paraná Magmatic Province. The black stars represent the location of the samples from this study. Modified from Peate et al. (1992) and Janasi et al. (2011). Abbreviations – Par: Paraná, Ete: Etendeka, Tr: Trindade, TC: Tristán da Cunha.

Figure 2 – Binary plots of (a) Mg# vs Ti (ppm), (b) Mg# vs Ti/Y, (c) La/Yb vs Ti/Y and (d) Sm/Yb vs Ti/Y for various samples from the PMP. Note the general geochemical separation of the samples with higher Ti contents and Ti/Y ratios from those with lower values. Whole-rock results are given in electronic materials (ESM, Table 1).

Figure 3 - Binary plots of (a) Al_2O_3, (b) Fe_2O_3, (c) CaO, (d) Ni, (e) Cr and (f) Cu versus Mg# for various samples from the PMP. The fractionation trends are compatible with the progressive crystallization of olivine, pyroxene, plagioclase and chromite. The increase in Cu concentrations following fractionation is in agreement with its incompatible behaviour, whereas lower concentrations support sulfide removal. Whole-rock results are given in electronic materials (ESM, Table 1).

Figure 4 - Binary plots of (a) Pt, (b) Pd, (c) Rh, (d) Ru, (e) Ir and (f) Os versus Mg# for various samples from the PMP. The back arrows indicate the processes variably affecting the distribution of PGE in the samples. Please see text for further explanation. Dashed lines indicate the detection limits. Whole-rock results are given in electronic materials (ESM, Table 1).

609 **Figure 5 -** Binary plots of (a) Se, (b) Te, (c) Bi, (d) As and (e) Sb versus Mg# for
610 various samples from the PMP. Compositional fields of samples from other LIP and
611 MORB from Barnes and Mansur (*in press*) are shown for reference. There is no clear
612 correlation between Se, Te and Bi with Mg#, whereas Sb, and to a lesser extent As,
613 show a negative correlation with Mg#, thus supporting their incompatible behaviour
614 during fractionation. Dashed lines indicate the detection limits. Whole-rock results are
615 given in electronic materials (ESM, Table 1).

616 **Figure 6 -** Primitive mantle-normalized Ni–PGE–Au-Cu patterns of samples from (a)
617 high-Ti flows, (b) low-Ti flows, (c) Ponta Grossa dyke swarm and (d) Florianópolis
618 dyke swarm. Compositional fields for results from Mincato (2000) and Rocha-Júnior
619 et al. (2012) are shown for reference. Primitive mantle values from Lyubetskaya and
620 Korenaga (2007). Dashed lines indicate the detection limits. Whole-rock results are
621 given in electronic materials (ESM, Table 1).

622 **Figure 7 -** Binary plots of (a) Pt vs Pd, (b) Pd vs Rh, (c) Pd vs Ir, (d) Ru vs Rh, (e) Os
623 vs Ru and (f) Os vs Ir for various samples from the PMP. Black lines indicate different
624 Pt/Pd and Pd/Ir ratios on (a) and (c), respectively. Dashed lines indicate the detection
625 limits. Note that some previous analyses from literature have lower detection limits
626 than this study, and thus plot below dashed lines. Whole-rock results are given in
627 electronic materials (ESM, Table 1).

628 **Figure 8 -** Primitive mantle-normalized Th, Nb, Cu, TABS+, Pd and Pt patterns of
629 samples from (a) high-Ti flows, (b) low-Ti flows, (c) Ponta Grossa dyke swarm and
630 (d) Florianópolis dyke swarm. Primitive mantle values from Lyubetskaya and
631 Korenaga (2007). Black dashed lines indicate the detection limits, whereas black full

lines indicate the connection between Nb and Pd. Whole-rock results are given in electronic materials (ESM, Table 1).

Figure 9 – Binary plots of (a) Ir versus Cr and (b) Pd/Ir versus Ir for samples from the PMP. The gray X symbols are the results from Emeishan, Karoo, Siberian Traps from Barnes and Mansur (*in press*). The black line indicates the fractionation trend by the progressive crystallization of olivine and chromite leading to lower Ir contents and higher Pd/Ir ratios accompanied by lower Cr contents. Primitive mantle values (blue diamond) from Lyubetskaya and Korenaga (2007). Dashed line indicates the detection limit for Ir.

Figure 10 - Binary plots of (a) S vs Se, (b) Pd, (c) Te, (d) Bi and (e) Sb versus Se and (f) As vs Sb for various samples from the PMP. Compositional fields of samples from other LIP and MORB from Barnes and Mansur (*in press*) are shown for reference. Black line represents primitive mantle ratio (Lyubetskaya and Korenaga, 2007) and dashed lines indicate the detection limits. Whole-rock results are given in electronic materials (ESM, Table 1).

Figure 11 - Binary plot of Cu/Pd versus Pd for samples from the PMP. The black line corresponds to the product of bulk crystallization with sulfide liquid removal in cotectic proportions from an initial silicate liquid containing 15 ppb Pd and 160 ppm Cu. We used the partition coefficients for Pd and Cu between silicate and sufide liquid of 400000 and 1500, respectively (Mungall and Brenan, 2014). Please see text for further explanation.

Figure 12 - Binary plots of (a) Se, (b) Te, (c) Bi versus Cu and (d) As and (e) Sb versus Th for various samples from the PMP. Compositional fields of samples from other LIP and MORB from Barnes and Mansur (*in press*) are shown for reference. Black lines

represent primitive mantle ratio (Lyubetskaya and Korenaga, 2007) and dashed lines indicate the detection limits. Please see text for further explanation on the meaning of the ratios.

Electronic supplementary materials – Data availability

Table 1 - Whole-rock results obtained in this study.

Table 2 - Analyses of reference materials used to monitor the data quality of HG-AFS analyses.

Table 3 - Analyses of reference materials used to monitor the data quality of PGE, Au and S analyses.

Table 4 - Analyses of reference materials used to monitor the data quality of whole-rock analyses of major oxides and trace elements.

References

Almeida, V.V., Janasi, V.A., Heaman, L.M., Shaulis, B.J., Hollanda, M.H.B., Renne, P. R., 2018. Contemporaneous alkaline and tholeiitic magmatism in the Ponta Grossa Arch, Paraná-Etendeka Magmatic Province: Constraints from U–Pb zircon/baddeleyite and $^{40}Ar/^{39}Ar$ phlogopite dating of the José Fernandes Gabbro and mafic dykes. Journal of Volcanology and Geothermal Research 355, 55-65.

Arena, K. R., Hartmann, L. A., Baggio, S. B., 2014. Geological controls of copper, gold and silver in the Serra Geral Group, Realeza region, Paraná, Brazil. Ore Geology Reviews 63, 178-200.

Arguin, J.P., Pagé, P., Barnes, S.J., Yu, S.Y., Song, X.Y., 2016. The effect of chromite crystallization on the distribution of osmium, iridium, ruthenium and rhodium in picritic magmas: an example from the Emeishan Large Igneous Province, Southwestern China. Journal of Petrology 57(5), 1019-1048.

Baggio, S. B., Hartmann, L. A., Lazarov, M., Massonne, H. J., Opitz, J., Theye, T., Viefhaus, T., 2018. Origin of native copper in the Paraná volcanic province, Brazil,

integrating Cu stable isotopes in a multi-analytical approach. Mineralium Deposita 53(3), 417-434.

Barnes, S-J., Naldrett, A.J., Gorton, M.P., 1985. The origin of the fractionation of platinum-group elements in terrestrial magmas. Chemical geology 53(3-4), 303-323.

Barnes, S-J., Couture, J.F., Sawyer, E.W., Bouchaib, C., 1993. Nickel-copper occurrences in the Belleterre-Angliers Belt of the Pontiac Subprovince and the use of Cu-Pd ratios in interpreting platinum-group element distributions. Economic Geology 88(6), 1402-1418.

Barnes, S-J., Mansur, E.T., *in press.* Distribution of Te, As, Bi, Sb and Se (TABS+) in: Picrites and Basalts from Large Igneous Provinces; MORB, and Komatiites: Implications for the Formation of Magmatic Ni-Cu-PGE Deposits. Economic Geology.

Beccaluva, L., Bianchini, G., Natali, C., Siena, F., 2020. Plume-related Paranà-Etendeka igneous province: An evolution from plateau to continental rifting and breakup. Lithos, 105484.

Bédard, L.P., Savard, D., Barnes, S.J., 2008. Total sulfur concentration in geological reference materials by elemental infrared analyser. Geostandards and Geoanalytical Research 32(2), 203-208.

Bennio, L., Brotzu, P., d'Antonio, M., Feraud, G., Gomes, C.B., Marzoli, A., Ruberti, E., 2003. The tholeiitic dyke swarm of the Arraial do Cabo peninsula (SE Brazil): $^{39}Ar/^{40}Ar$ ages, petrogenesis, and regional significance. Journal of South American Earth Sciences 16(2), 163-176.

Bockrath, C., Ballhaus, C., Holzheid, A., 2004. Fractionation of the platinum-group elements during mantle melting. Science 305(5692), 1951-1953.

Callegaro, S., Baker, D.R., De Min, A., Marzoli, A., Geraki, K., Bertrand, H., Nestola, F., 2014. Microanalyses link sulfur from large igneous provinces and Mesozoic mass extinctions. Geology 42(10), 895-898.

Chen, L. M., Song, X. Y., Keays, R. R., Tian, Y. L., Wang, Y. S., Deng, Y. F., Xiao, J. F., 2013. Segregation and fractionation of magmatic Ni-Cu-PGE sulfides in the western Jinchuan intrusion, northwestern China: Insights from platinum group element geochemistry. Economic Geology 108(8), 1793-1811.

717 Crocket, J.H., 2002. Platinum-group element geochemistry of mafic and ultramafic
718 rocks. In: Cabri, L.J. (Ed.), Geology, Geochemistry, Mineralogy and Mineral
719 Beneficiation of Platinum-Group Ele- ments, 54. Canadian Institute of Mining,
720 Metallurgy and Petroleum, Special Volume, Montreal, Quebec, pp. 177–210.

721 Day, J.M., Pearson, D.G., Hulbert, L.J., 2013. Highly siderophile element behaviour
722 during flood basalt genesis and evidence for melts from intrusive chromitite
723 formation in the Mackenzie large igneous province. Lithos 182, 242-258.

724 Edmonds, M., Mather, T.A., Liu, E.J., 2018. A distinct metal fingerprint in arc volcanic
725 emissions. Nature Geosciences 11(10), 790-794.

726 Ewart, A., Marsh, J.S., Milner, S.C., Duncan, A.R., Kamber, B.S., Armstrong, R.A.,
727 2004. Petrology and geochemistry of Early Cretaceous bimodal continental flood
728 volcanism of the NW Etendeka, Namibia. Part 1: Introduction, mafic lavas and re-
729 evaluation of mantle source components. Journal of Petrology 45(1), 59-105.

730 Finnigan, C.S., Brenan, J.M., Mungall, J.E., McDonough, W.F., 2008. Experiments and
731 models bearing on the role of chromite as a collector of platinum group minerals by
732 local reduction. Journal of Petrology 49(9), 1647-1665.

733 Florisbal, L.M., Heaman, L.M., de Assis Janasi, V., de Fatima Bitencourt, M., 2014.
734 Tectonic significance of the Florianópolis dyke Swarm, Paraná–Etendeka Magmatic
735 Province: a reappraisal based on precise U–Pb dating. Journal of Volcanology and
736 Geothermal Research 289, 140-150.

737 Fodor, R.V., McKee, E.H., Roisenberg, A., 1989. Age distribution of Serra Geral
738 (Paraná) flood basalts, southern Brazil. Journal of South American earth
739 sciences 2(4), 343-349.

740 Forrest, A., Keller, K.A., Schilling, J.G., 2017. Selenium, tellurium and sulfur variations
741 in basalts along the Reykjanes Ridge and extension over Iceland, from 50ºN to
742 65ºN. Interdisciplinary Earth Data Alliance (IEDA), Palisades, NY.

743 Frank, H.T., Gomes, M.E.B., Formoso, M.L.L., 2009. Review of the areal extent and
744 the volume of the Serra Geral Formation, Paraná Basin, South America. Pesquisas
745 em Geociências 36(1), 49-57.

746 Ganino, C., Arndt, N.T., 2009. Climate changes caused by degassing of sediments
747 during the emplacement of large igneous provinces. Geology 37(4), 323-326.

748 Garda, G.M., Schorscher, H.D., Esperanca, S., Carlson, R.W., 1995. The petrology and
749 geochemistry of coastal dikes from Sao Paulo State, Brazil: implications for variable
750 lithospheric contributions to alkaline magmas from the Western margin of South
751 Atlantic. Anais da Academía brasileira de Ciências 67, 191-216.

752 Guimarães, L.F., Hornby, A., Kueppers, U., Alves, A., de Assis Janasi, V., Dingwell,
753 D.B., 2019. Generation of block-and-ash flows at the onset of silicic volcanism in
754 the Paraná Magmatic Province (Brazil): evidence from photoanalysis of Caxias do
755 Sul breccias. Bulletin of Volcanology 81(11), 65.

756 Harris, C., 1987. A note on native copper occurrences in Karoo basalts of the Etendeka
757 Formation. Communications of the Geological Survey of Namibia 3, 139-140.

758 Heimdal, T.H., Callegaro, S., Svensen, H.H., Jones, M.T., Pereira, E., Planke, S., 2019.
759 Evidence for magma–evaporite interactions during the emplacement of the Central
760 Atlantic Magmatic Province (CAMP) in Brazil. Earth and Planetary Science
761 Letters 506, 476-492.

762 Hughes, H.S., McDonald, I., Kerr, A.C., 2015. Platinum-group element signatures in
763 the North Atlantic Igneous Province: Implications for mantle controls on metal
764 budgets during continental breakup. Lithos 233, 89-110.

765 Janasi, V., de Freitas, V.A., Heaman, L.H., 2011. The onset of flood basalt volcanism,
766 Northern Paraná Basin, Brazil: A precise U–Pb baddeleyite/zircon age for a
767 Chapecó-type dacite. Earth and Planetary Science Letters 302(1-2), 147-153.

768 Jenner, F.E., O'Neill, H.S.C., 2012. Analysis of 60 elements in 616 ocean floor basaltic
769 glasses. Geochemistry, Geophysics Geosystems 13, Q0200.

770 Jennings, E.S., Gibson, S.A., Maclennan, J., 2019. Hot primary melts and mantle source
771 for the Paraná-Etendeka flood basalt province: New constraints from Al-in-olivine
772 thermometry. Chemical Geology 529, 119287.

773 Jowitt, S.M., Ernst, R.E., 2013. Geochemical assessment of the metallogenic potential
774 of Proterozoic LIPs of Canada. Lithos 174, 291-307.

775 König, S., Luguet, A., Lorand, J-P., Wombacher, F., Lissner, M., 2012. Selenium and
776 tellurium systematics of the Earth's mantle from high precision analyses of ultra-
777 depleted orogenic peridotites. Geochimica et Cosmochimica Acta 86, 354-366.

778 Li, C., Ripley, E. M., 2005. Empirical equations to predict the sulfur content of mafic
779 magmas at sulfide saturation and applications to magmatic sulfide
780 deposits. Mineralium Deposita 40(2), 218-230.

781 Li C., Boudreau, A.E., 2017. The origin of high-Cu/S sulfides by shallow level
782 degassing in the Skaergaard intrusion, East Greenland. Geology 45, 1075-1078.

783 Liu, Y., Brenan, J., 2015. Partitioning of platinum-group elements (PGE) and
784 chalcogens (Se, Te, As, Sb, Bi) between monosulfide-solid solution (MSS),
785 intermediate solid solution (ISS) and sulfide liquid at controlled fO2–fS2
786 conditions. Geochimica et Cosmochimica Acta 159, 139-161.

787 Lightfoot, P.C., Naldrett, A.J., Gorbachev, N.S., Fedorenko, V.A., Hawkesworth, C.J.,
788 Hergt, J., Doherty, W., 1994. Chemostratigraphy of Siberian Trap lavas, Noril'sk
789 district, Russia: Implications for the source of flood basalt magmas and their
790 associated Ni-Cu mineralization. Ontario Geological Survey Special Publications 5,
791 283-312.

792 Lissner, M., König, S., Luguet, A., Le Roux, P., Schuth, S., Heuser, A., le Roex, A.P.,
793 2014. Selenium and tellurium systematics in MORBs from the southern Mid-Atlantic
794 Ridge (47–50 S). Geochimica et Cosmochimica Acta 144, 379-402.

795 Locmelis, M., Pearson, N.J., Barnes, S.J., Fiorentini, M.L., 2011. Ruthenium in
796 komatiitic chromite. Geochimica et Cosmochimica Acta 75, 3645–3661.

797 Lodders, K., 2003. Solar system abundances and condensation temperatures of the
798 elements. The Astrophysical Journal 591(2), 1220.

799 Lyubetskaya T., Korenaga, J., 2007. Chemical composition of Earth's primitive mantle
800 and its variance: 1. Method and results. Journal of Geophysical Research 112,
801 B03211.

802 Maciag, B.J., Brenan, J.M., 2020. Speciation of Arsenic and Antimony in Basaltic
803 Magmas. Geochimica et Cosmochimica Acta 276, 198-218.

804 Maier, W.D., Barnes, S.J., De Klerk, W.J., Teigler, B., Mitchell, A.A., 1996. Cu/Pd and
805 Cu/Pt of silicate rocks in the Bushveld Complex; implications for platinum-group
806 element exploration. Economic Geology 91(6), 1151-1158.

807 Maier, W.D., Barnes, S.J., Marsh, J.S., 2003. The concentrations of the noble metals in
808 Southern African flood-type basalts and MORB: implications for petrogenesis and

809 magmatic sulphide exploration. Contributions to Mineralogy and Petrology 146(1),
810 44-61.

811 Mansur, E.T., Barnes, S-J., 2020a. The role of Te, As, Bi, Sn and Sb during the
812 formation of PGE deposits: examples from the Bushveld and Stillwater Complexes.
813 Geochimica et Cosmochimica Acta 272, 235-258.

814 Mansur, E.T., Barnes, S.J., 2020b. Concentrations of Te, As, Bi, Sb and Se in the
815 marginal zone of the Bushveld complex: Evidence for crustal contamination and the
816 nature of the magma that formed the Merensky Reef. Lithos 358-359, 105407.

817 Mansur, E.T., Barnes, S-J., Duran, C.J., 2020a. Distribution of chalcophile and
818 platinum-group elements among pyrrhotite, pentlandite, chalcopyrite and cubanite
819 from the Noril'sk-Talnakh ores: implications for the formation of platinum-group
820 minerals. Mineralium Deposita 55, 1215–1232

821 Mansur, E.T., Barnes, S-J., Savard, D., Webb, P.C., 2020b. Determination of Te, As,
822 Bi, Sb and Se (TABS) in Geological Reference Materials and GeoPT Proficiency
823 Test Materials by Hydride Generation-Atomic Fluorescence Spectrometry (HG-
824 AFS). Geostandards and Geoanalytical Research 44(1), 147-167.

825 Mantovani, M.S.M., Marques, L.S., De Sousa, M.A., Civetta, L., Atalla, L., Innocenti,
826 F., 1985. Trace element and strontium isotope constraints on the origin and evolution
827 of Paraná continental flood basalts of Santa Catarina State (southern Brazil). Journal
828 of Petrology 26(1), 187-209.

829 Marsh, J.S., Swart, R., 2018. The Bero Volcanic Complex: extension of the Paraná-
830 Etendeka Igneous Province into SW Angola. Journal of Volcanology and
831 Geothermal Research 355, 21-31.

832 Mathez, E.A., 1976. Sulfur solubility and magmatic sulfides in submarine basalt glass.
833 Journal of Geophysical Research 81, 4269-4276.

834 Mincato, R.L., 2000. Metalogenia dos elementos do grupo da platina com base na
835 estratigrafia e geoquímica da Província Ígnea Continental do Paraná. Unpublished
836 M.Sc. thesis, Unicamp.

837 Mori, P.E., Correia, C.T., Reeves, S., Haukka, M., 1999. Development of a fused glass
838 disc XRF facility and comparison with the pressed powder pellet technique at

839 Instituto de Geociências, São Paulo University, Brazil. Revista Brasileira de
840 Geociências 29(3), 441-446.

841 Mungall, J.E., Brenan, J.M., 2014. Partitioning of platinum-group elements and Au
842 between sulfide liquid and basalt and the origins of mantle-crust fractionation of the
843 chalcophile elements. Geochimica et Cosmochimica Acta 125, 265-289.

844 Navarro, M.S., Andrade, S., Ulbrich, H., Gomes, C.B., Girardi, V.A., 2008. The direct
845 determination of rare earth elements in basaltic and related rocks using ICP-MS:
846 Testing the efficiency of microwave oven sample decomposition
847 procedures. Geostandards and Geoanalytical Research 32(2), 167-180.

848 Pagé, P., Barnes, S.J., Bédard, J.H., Zientek, M.L., 2012. In situ determination of Os, Ir,
849 and Ru in chromites formed from komatiite, tholeiite and boninite magmas:
850 implications for chromite control of Os, Ir and Ru during partial melting and crystal
851 fractionation. Chemical Geology 302, 3-15.

852 Park, J.W., Kamenetsky, V., Campbell, I., Park, G., Hanski, E., Pushkarev, E., 2017.
853 Empirical constraints on partitioning of platinum group elements between Cr-spinel
854 and primitive terrestrial magmas. Geochimica et Cosmochimica Acta 216, 393-416.

855 Patten, C., Barnes, S-J., Mathez, E.A., Jenner, F.E., 2013. Partition coefficients of
856 chalcophile elements between sulfide and silicate melts and the early crystallization
857 history of sulfide liquid: LA-ICP-MS analysis of MORB sulfide droplets. Chemical
858 Geology 358, 170–188.

859 Peate, D.W., Hawkesworth, C.J., Mantovani, M.S., 1992. Chemical stratigraphy of the
860 Paraná lavas (South America): classification of magma types and their spatial
861 distribution. Bulletin of Volcanology 55(1-2), 119-139.

862 Peate, D.W., Hawkesworth, C.J., 1996. Lithospheric to asthenospheric transition in low-
863 Ti flood basalts from southern Parana, Brazil. Chemical Geology 127(1-3), 1-24.

864 Peate, D. W., 1997. The parana-etendeka province. Geophysical Monograph-American
865 Geophysical Union 100, 217-246.

866 Pinto, V.M., Hartmann, L.A., Santos, J.O.S., McNaughton, N.J., Wildner, W., 2011a.
867 Zircon U–Pb geochronology from the Paraná bimodal volcanic province support a
868 brief eruptive cycle at~ 135 Ma. Chemical Geology 281(1-2), 93-102.

869 Pinto, V. M., Hartmann, L. A., Wildner, W., 2011b. Epigenetic hydrothermal origin of
870 native copper and supergene enrichment in the Vista Alegre district, Paraná basaltic
871 province, southernmost Brazil. International Geology Review 53(10), 1163-1179.

872 Pitcher, L., Helz, R. T., Walker, R. J., Piccoli, P., 2009. Fractionation of the platinum-
873 group elments and Re during crystallization of basalt in Kilauea Iki Lava Lake,
874 Hawaii. Chemical Geology 260(3-4), 196-210.

875 Polo, L.A., Giordano, D., Janasi, V.A., Guimarães, L.F., 2018. Effusive silicic
876 volcanism in the Paraná Magmatic Province, South Brazil: Physico-chemical
877 conditions of storage and eruption and considerations on the rheological behavior
878 during emplacement. Journal of Volcanology and Geothermal Research 355, 115-
879 135.

880 Queffurus, M., Barnes, S.J., 2015. A review of sulfur to selenium ratios in magmatic
881 nickel–copper and platinum-group element deposits. Ore Geology Reviews 69, 301-
882 324.

883 Righter, K., Campbell, A.J., Humayun, M., Hervig, R.L., 2004. Partitioning of Ru, Rh,
884 Pd, Re, Ir, and Au between Cr-bearing spinel, olivine, pyroxene and silicate
885 melts. Geochimica et Cosmochimica Acta 68(4), 867-880.

886 Rocha-Júnior, E.R., Puchtel, I.S., Marques, L.S., Walker, R.J., Machado, F.B., Nardy,
887 A.J., Figueiredo, A.M., 2012. Re–Os isotope and highly siderophile element
888 systematics of the Paraná continental flood basalts (Brazil). Earth and Planetary
889 Science Letters 337, 164-173.

890 Rocha-Júnior, E.R., Marques, L.S., Babinski, M., Nardy, A.J., Figueiredo, A.M.,
891 Machado, F.B., 2013. Sr–Nd–Pb isotopic constraints on the nature of the mantle
892 sources involved in the genesis of the high-Ti tholeiites from northern Paraná
893 Continental Flood Basalts (Brazil). Journal of South American Earth Sciences 46, 9-
894 25.

895 Romanini, S. J., Albuquerque, L. F. F. D., 2001. Geological, Geochemical and
896 Potentiality Aspects of Ni-Cu-PGE Deposits of the Paraná Basin Magmatism.
897 Informe de Recursos Minerais - Série Metais do Grupo da Platina e Associados, 29.

898 Rossetti, L., Lima, E.F., Waichel, B.L., Hole, M.J., Simões, M.S., Scherer, C.M., 2018.
899 Lithostratigraphy and volcanology of the Serra Geral Group, Paraná-Etendeka
900 Igneous Province in southern Brazil: Towards a formal stratigraphical
901 framework. Journal of Volcanology and Geothermal Research 355, 98-114.

902 Savard, D., Barnes, S.J., Meisel, T., 2010. Comparison between nickel-sulfur fire assay
903 Te co-precipitation and isotope dilution with high-pressure asher acid digestion for
904 the determination of platinum-group elements, rhenium and gold. Geostandards and
905 Geoanalytical Research 34(3), 281-291.

906 Self, S., Thordarson, T., Widdowson, M., 2005. Gas fluxes from flood basalt
907 eruptions. Elements 1(5), 283-287.

908 Thiede, D.S., Vasconcelos, P.M., 2010. Paraná flood basalts: rapid extrusion hypothesis
909 confirmed by new 40Ar/39Ar results. Geology 38(8), 747-750.

910 Thompson, R.N., Gibson, S.A., Dickin, A.P., Smith, P.M., 2001. Early Cretaceous
911 basalt and picrite dykes of the southern Etendeka region, NW Namibia: windows into
912 the role of the Tristan mantle plume in Paraná–Etendeka magmatism. Journal of
913 Petrology 42(11), 2049-2081.

914 Vandenbroucke, T.R., Emsbo, P., Munnecke, A., Nuns, N., Duponchel, L., Lepot, K.,
915 Kiessling, W., 2015. Metal-induced malformations in early Palaeozoic plankton are
916 harbingers of mass extinction. Nature Communications 6(1), 1-7.

917 Wallace, P.J., Edmonds, M., 2011. The sulfur budget in magmas: evidence from melt
918 inclusions, submarine glasses, and volcanic gas emissions. Reviews in Mineralogy
919 and Geochemistry 73(1), 215-246.

920 Wieser, P., Jenner, F., Edmonds, M., Maclennan, J., Kunz, B., 2020. Chalcophile
921 elements track the fate of sulfur at Kīlauea Volcano, Hawai'i. Geochimica et
922 Cosmochimica Acta 282, 245-275.

923 Wignall, P.B., 2001. Large igneous provinces and mass extinctions. Earth-Science
924 Reviews 53(1-2), 1-33.

925 Zelenski, M., Malik, N., Taran, Y., 2014. Emissions of trace elements during the 2012–
926 2013 effusive eruption of Tolbachik volcano, Kamchatka-enrichment factors,
927 partition coefficients and aerosol contribution. Journal of Volcanology and
928 Geothermal Research 285, 136-149.

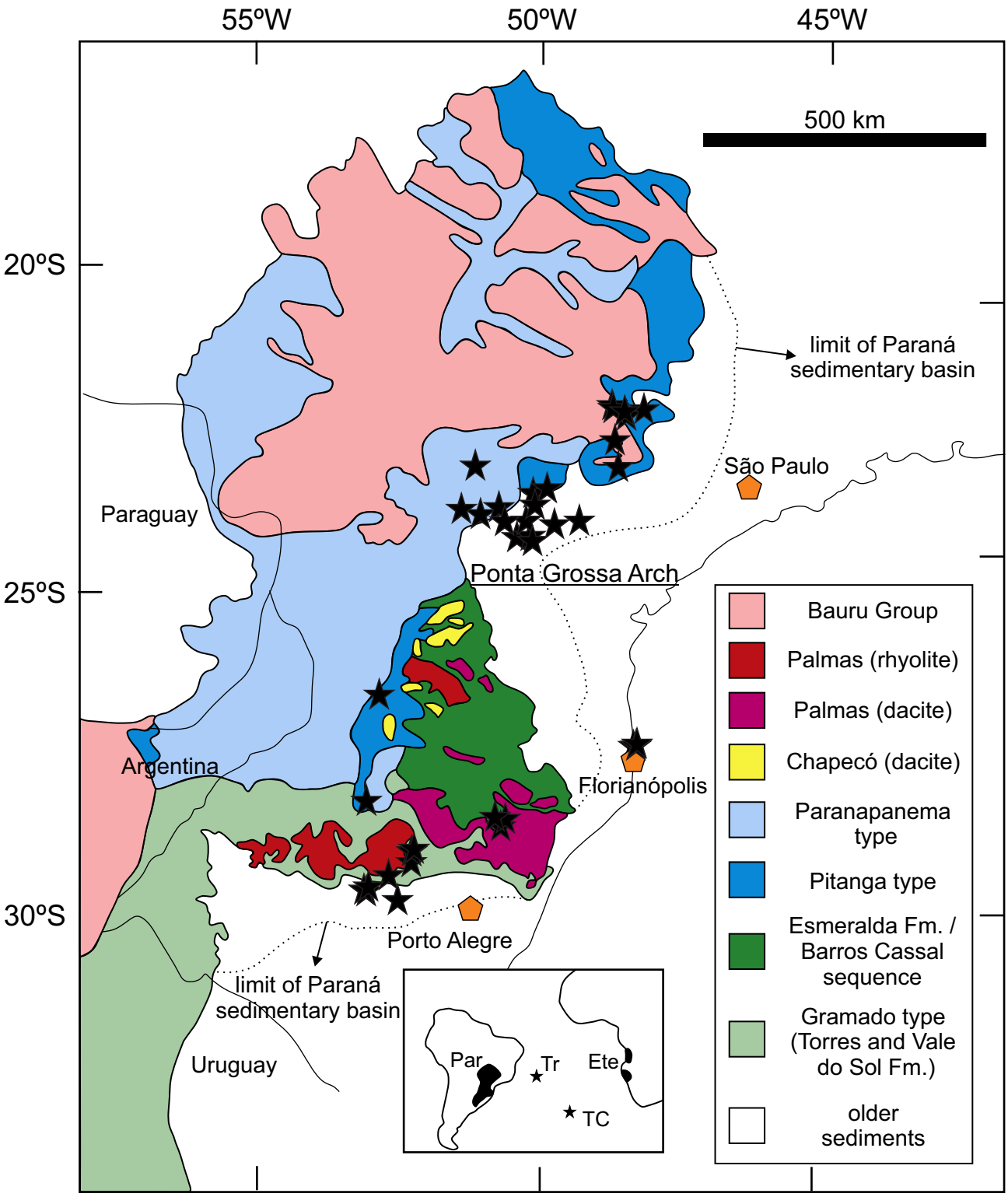
55ºW
50ºW
45ºW
20ºS
25ºS
30ºS
500 km
limit of Paraná sedimentary basin
São Paulo
Paraguay
Ponta Grossa Arch
Argentina
Florianópolis
Porto Alegre
limit of Paraná sedimentary basin
Uruguay
Par
Tr
Ete
TC
Bauru Group
Palmas (rhyolite)
Palmas (dacite)
Chapecó (dacite)
Paranapanema type
Pitanga type
Esmeralda Fm. / Barros Cassal sequence
Gramado type (Torres and Vale do Sol Fm.)
older sediments

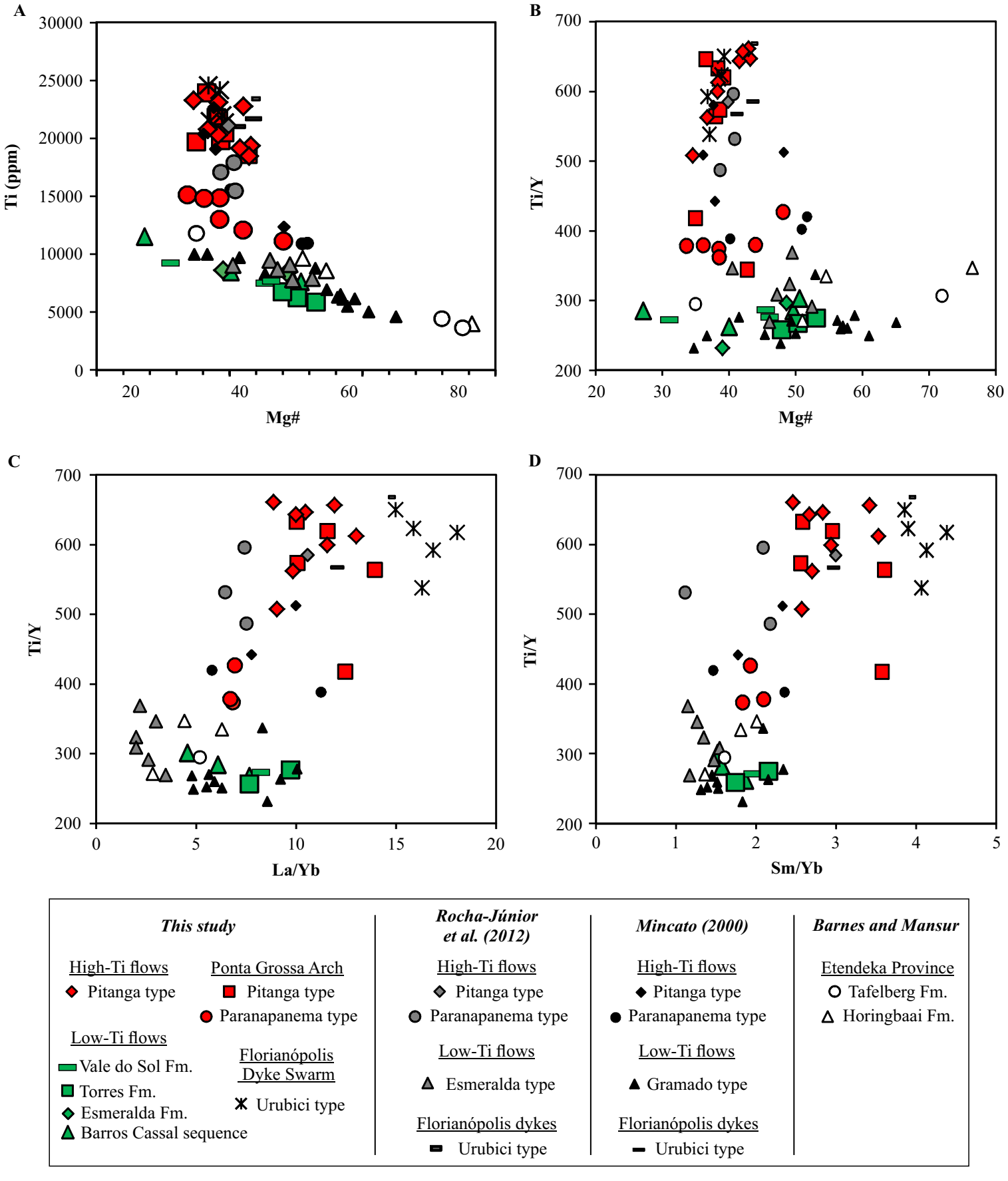
A
Ti (ppm)
Mg#
B
Ti/Y
Mg#
C
Ti/Y
La/Yb
D
Ti/Y
Sm/Yb
This study
High-Ti flows
Pitanga type
Ponta Grossa Arch
Pitanga type
Paranapanema type
Low-Ti flows
Vale do Sol Fm.
Torres Fm.
Esmeralda Fm.
Barros Cassal sequence
Florianópolis Dyke Swarm
Urubici type
Rocha-Júnior et al. (2012)
High-Ti flows
Pitanga type
Paranapanema type
Low-Ti flows
Esmeralda type
Florianópolis dykes
Urubici type
Mincato (2000)
High-Ti flows
Pitanga type
Paranapanema type
Low-Ti flows
Gramado type
Florianópolis dykes
Urubici type
Barnes and Mansur
Etendeka Province
Tafelberg Fm.
Horingbaai Fm.

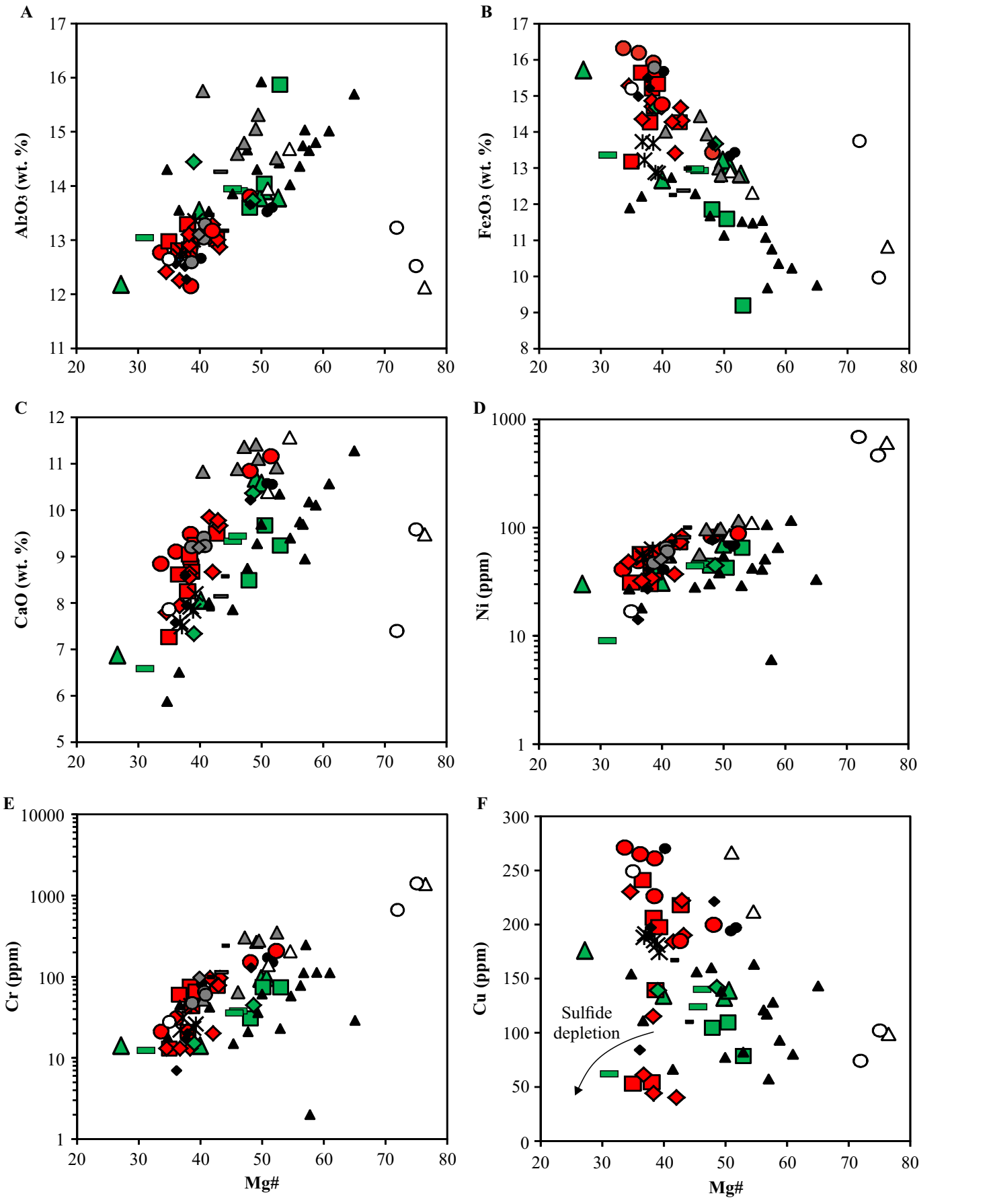

This study

<u>High-Ti flows</u>
- Pitanga type

<u>Ponta Grossa Arch</u>
- Pitanga type
- Paranapanema type

<u>Low-Ti flows</u>
- Vale do Sol Fm.
- Torres Fm.
- Esmeralda Fm.
- Barros Cassal sequence

<u>Florianópolis Dyke Swarm</u>
- Urubici type

Rocha-Júnior et al. (2012)

<u>High-Ti flows</u>
- Pitanga type
- Paranapanema type

<u>Low-Ti flows</u>
- Esmeralda type

<u>Florianópolis dykes</u>
- Urubici type

Mincato (2000)

<u>High-Ti flows</u>
- Pitanga type
- Paranapanema type

<u>Low-Ti flows</u>
- Gramado type

<u>Florianópolis dykes</u>
- Urubici type

Barnes and Mansur

<u>Etendeka Province</u>
- Tafelberg Fm.
- Horingbaai Fm.

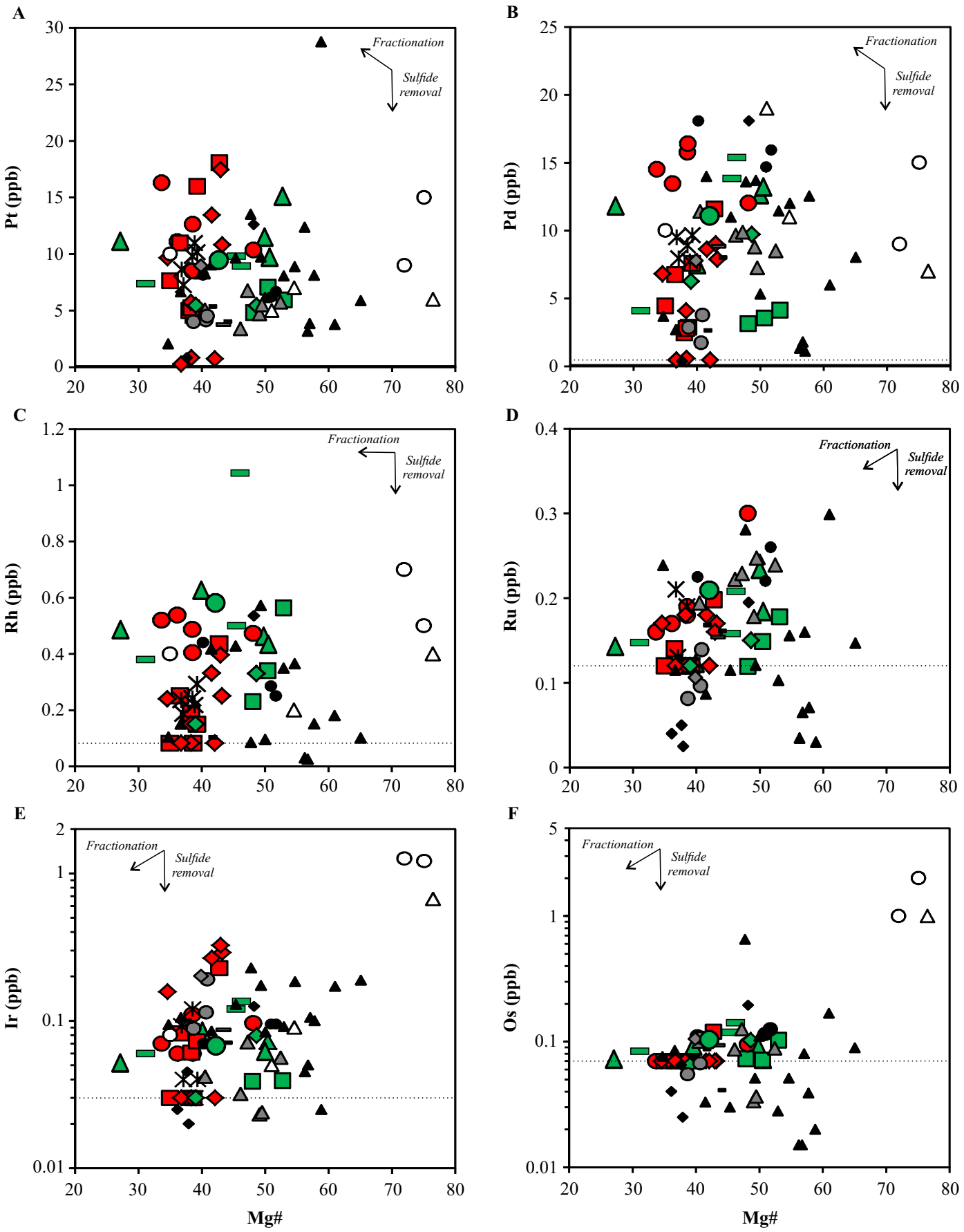

This study

High-Ti flows
- Pitanga type

Ponta Grossa Arch
- Pitanga type
- Paranapanema type

Low-Ti flows
- Vale do Sol Fm.
- Paranapanema type
- Torres Fm.
- Esmeralda Fm.
- Barros Cassal sequence

Florianópolis Dyke Swarm
- Urubici type

Rocha-Júnior et al. (2012)

High-Ti flows
- Pitanga type
- Paranapanema type

Low-Ti flows
- Esmeralda type

Florianópolis dykes
- Urubici type

Mincato (2000)

High-Ti flows
- Pitanga type
- Paranapanema type

Low-Ti flows
- Gramado type

Florianópolis dykes
- Urubici type

Mansur and Barnes (20XX)

Etendeka Province
- Tafelberg Fm.
- Horingbaai Fm.

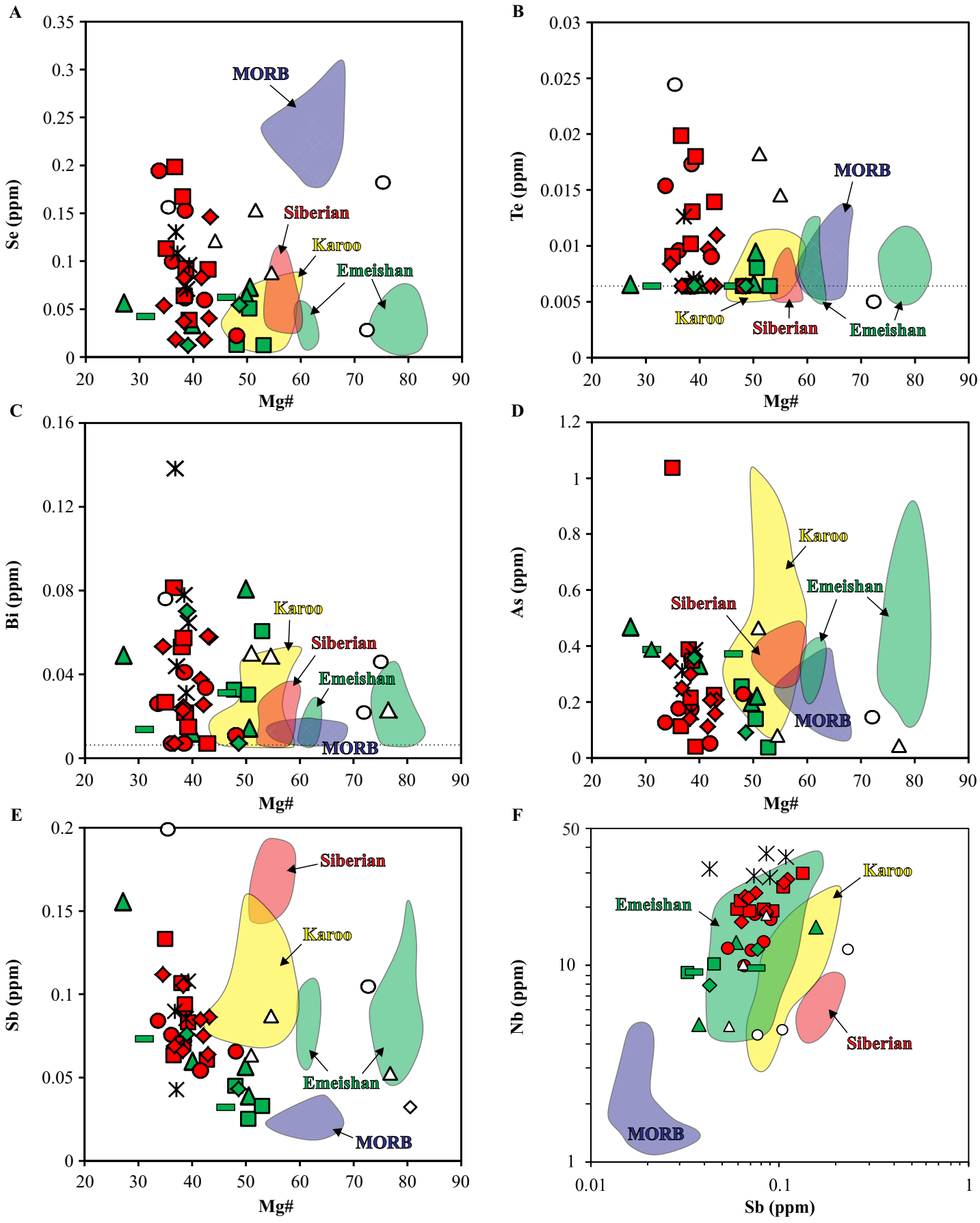

This study

High-Ti flows
- Pitanga type

Low-Ti flows
- Vale do Sol Fm.
- Torres Fm.
- Esmeralda Fm.
- Barros Cassal sequence

Ponta Grossa Arch
- Pitanga type
- Paranapanema type

Florianópolis Dyke Swarm
- Urubici type

Barnes and Mansur

Etendeka Province
- Tafelberg Fm.
- Horingbaai Fm.

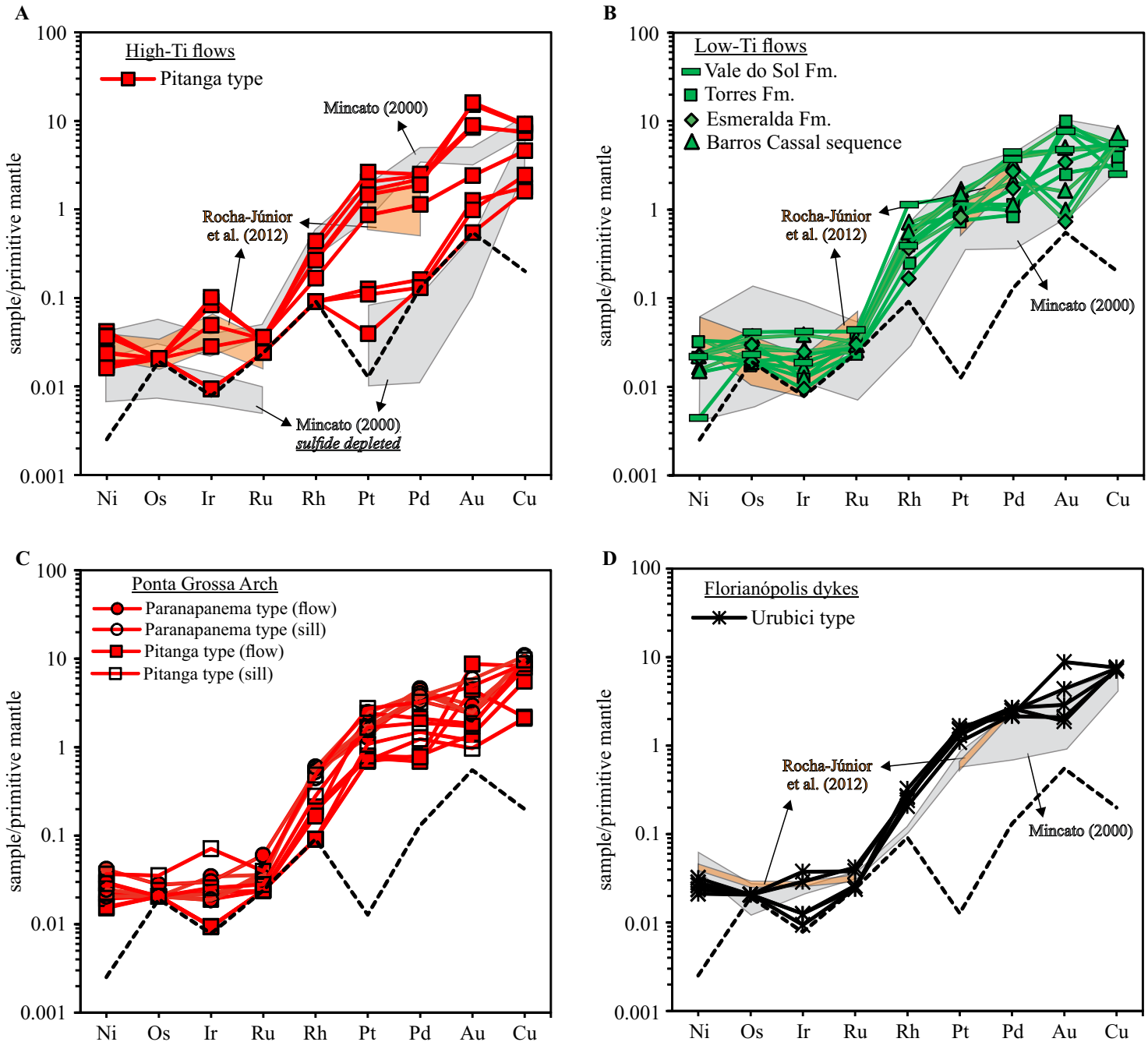
A
High-Ti flows
Pitanga type
Mincato (2000)
Rocha-Júnior et al. (2012)
Mincato (2000)
sulfide depleted
sample/primitive mantle
100
10
1
0.1
0.01
0.001
Ni
Os
Ir
Ru
Rh
Pt
Pd
Au
Cu
B
Low-Ti flows
Vale do Sol Fm.
Torres Fm.
Esmeralda Fm.
Barros Cassal sequence
Rocha-Júnior et al. (2012)
Mincato (2000)
C
Ponta Grossa Arch
Paranapanema type (flow)
Paranapanema type (sill)
Pitanga type (flow)
Pitanga type (sill)
D
Florianópolis dykes
Urubici type
Rocha-Júnior et al. (2012)
Mincato (2000)

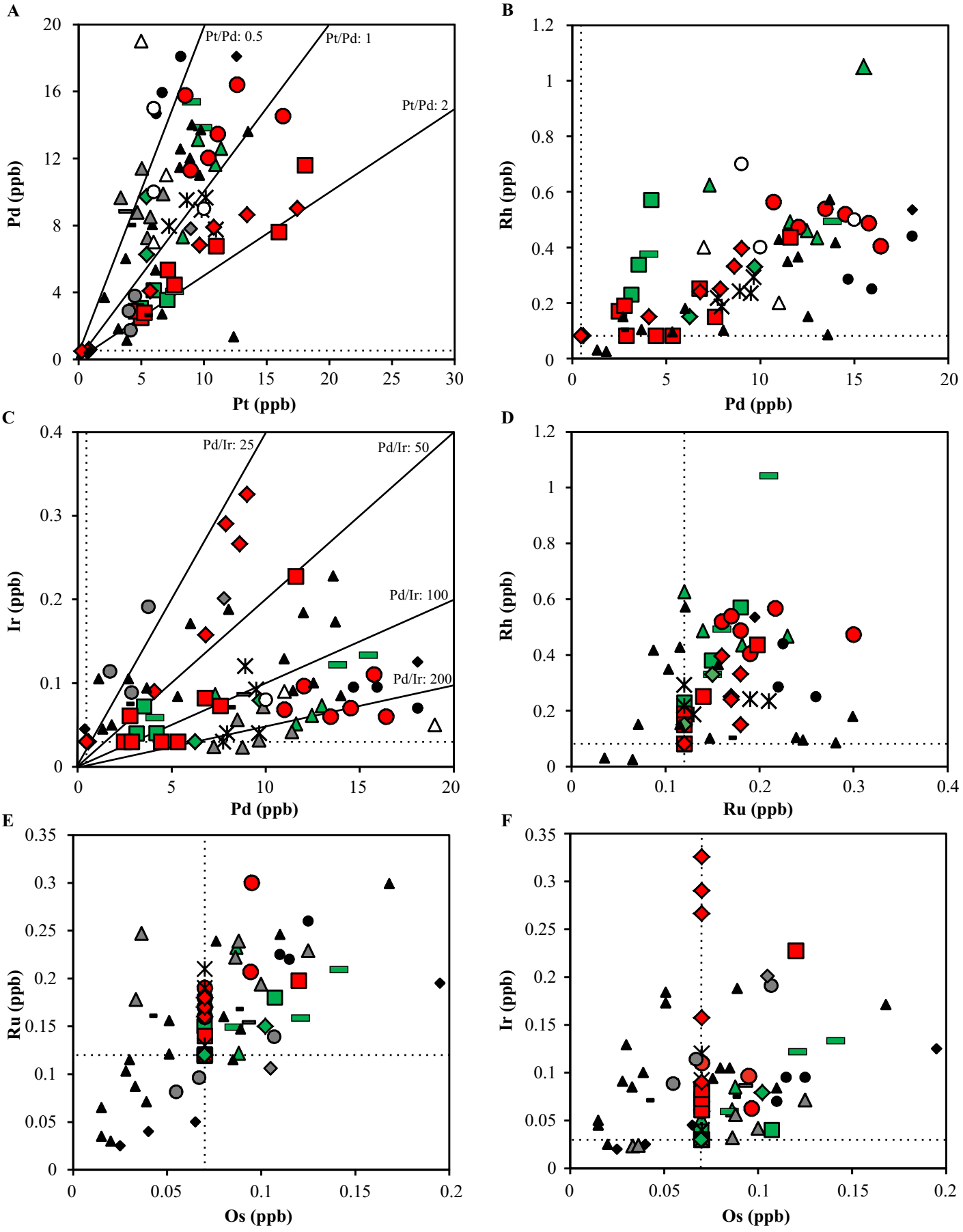

This study

High-Ti flows
- Pitanga type

Ponta Grossa Arch
- Pitanga type
- Paranapanema type

Low-Ti flows
- Vale do Sol Fm.
- Torres Fm.
- Esmeralda Fm.
- Barros Cassal sequence

Florianópolis Dyke Swarm
- Urubici type

Rocha-Júnior et al. (2012)

High-Ti flows
- Pitanga type
- Paranapanema type

Low-Ti flows
- Esmeralda type

Florianópolis dykes
- Urubici type

Mincato (2000)

High-Ti flows
- Pitanga type
- Paranapanema type

Low-Ti flows
- Gramado type

Florianópolis dykes
- Urubici type

Barnes and Mansur

Etendeka Province
- Tafelberg Fm.
- Horingbaai Fm.

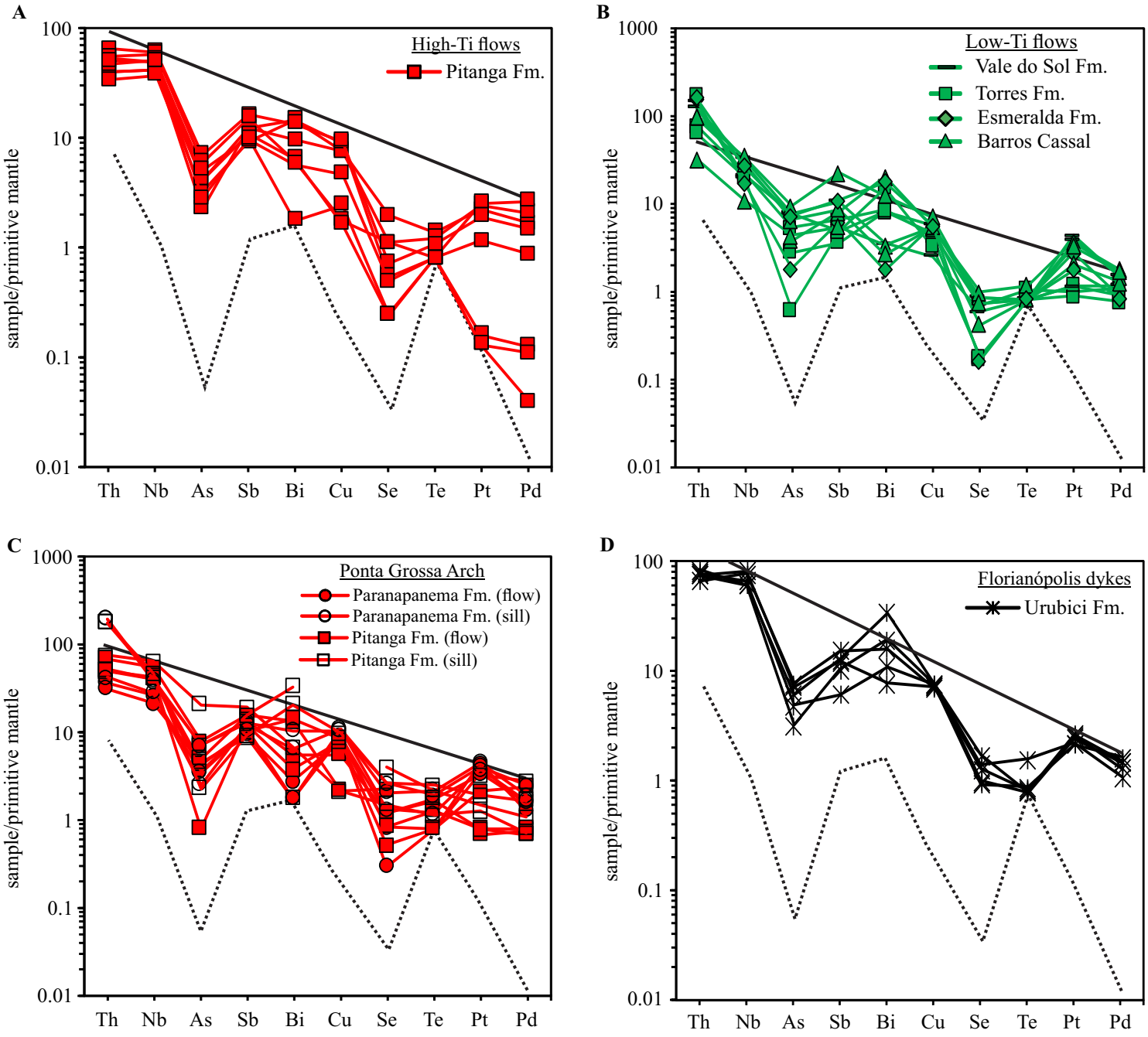
A
High-Ti flows
Pitanga Fm.
sample/primitive mantle
100
10
1
0.1
0.01
Th Nb As Sb Bi Cu Se Te Pt Pd
B
Low-Ti flows
Vale do Sol Fm.
Torres Fm.
Esmeralda Fm.
Barros Cassal
sample/primitive mantle
1000
100
10
1
0.1
0.01
Th Nb As Sb Bi Cu Se Te Pt Pd
C
Ponta Grossa Arch
Paranapanema Fm. (flow)
Paranapanema Fm. (sill)
Pitanga Fm. (flow)
Pitanga Fm. (sill)
sample/primitive mantle
1000
100
10
1
0.1
0.01
Th Nb As Sb Bi Cu Se Te Pt Pd
D
Florianópolis dykes
Urubici Fm.
sample/primitive mantle
100
10
1
0.1
0.01
Th Nb As Sb Bi Cu Se Te Pt Pd

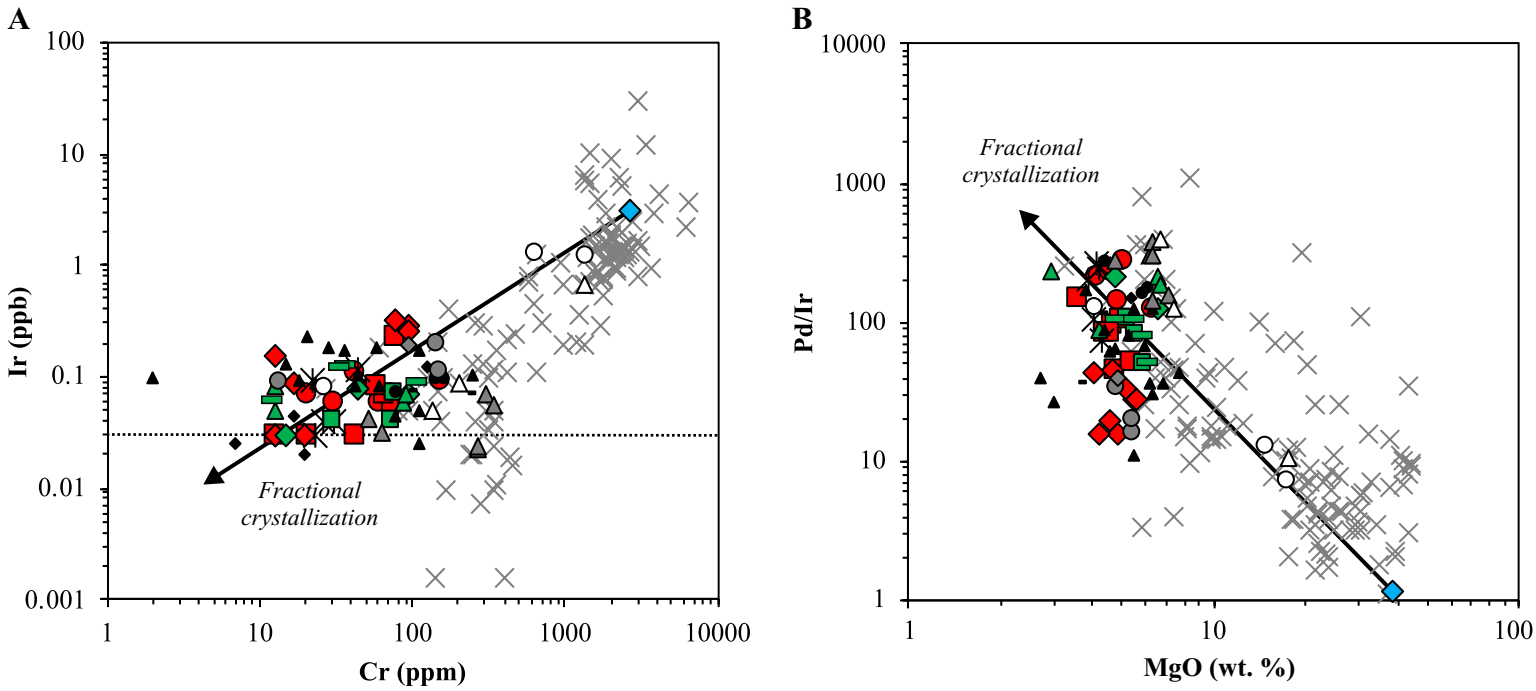

This study

High-Ti flows
- Pitanga type
- Paranapanema type

Ponta Grossa Arch
- Pitanga type

Low-Ti flows
- Vale do Sol Fm.
- Torres Fm.
- Esmeralda Fm.
- Barros Cassal sequence

Florianópolis Dyke Swarm
- Urubici type

Rocha-Júnior et al. (2012)

High-Ti flows
- Pitanga type
- Paranapanema type

Low-Ti flows
- Esmeralda type

Florianópolis dykes
- Urubici type

Mincato (2000)

High-Ti flows
- Pitanga type
- Paranapanema type

Low-Ti flows
- Gramado type

Florianópolis dykes
- Urubici type

Barnes and Mansur in press

Etendeka Province
- Tafelberg Fm.
- Horingbaai Fm.

Karroo, Emeishan Siberia, MORB

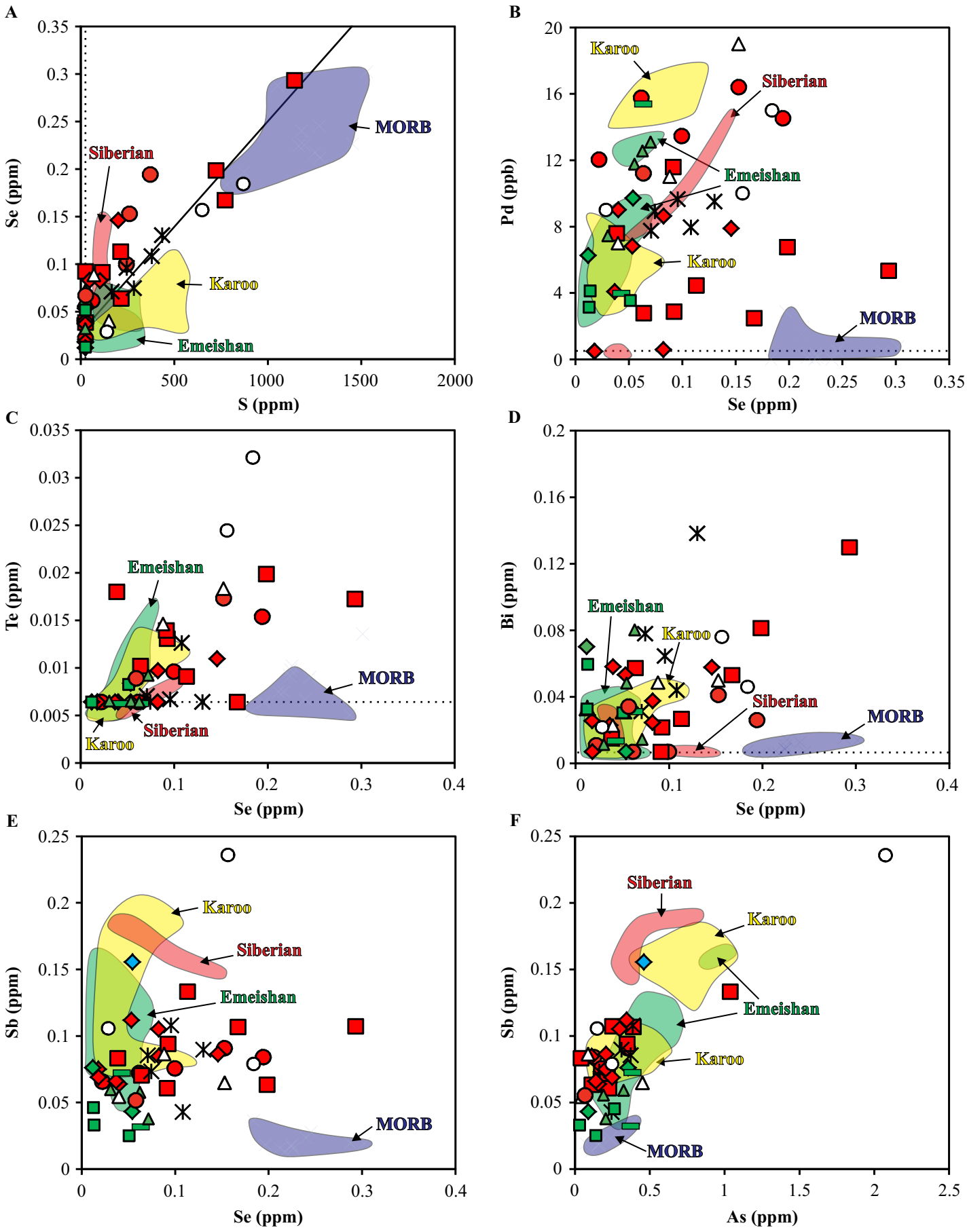
A
Se (ppm)
S (ppm)
Siberian
MORB
Karoo
Emeishan
B
Pd (ppb)
Se (ppm)
Karoo
Siberian
Emeishan
Karoo
MORB
C
Te (ppm)
Se (ppm)
Emeishan
MORB
Siberian
Karoo
D
Bi (ppm)
Se (ppm)
Emeishan
Karoo
Siberian
MORB
E
Sb (ppm)
Se (ppm)
Karoo
Siberian
Emeishan
MORB
F
Sb (ppm)
As (ppm)
Siberian
Karoo
Emeishan
Karoo
MORB
This study
High-Ti flows
Pitanga type
Ponta Grossa Arch
Pitanga type
Paranapanema type
Low-Ti flows
Vale do Sol Fm.
Torres Fm.
Esmeralda Fm.
Barros Cassal sequence
Florianópolis Dyke Swarm
Urubici type
Barnes and Mansur
Etendeka Province
Tafelberg Fm.
Horingbaai Fm.

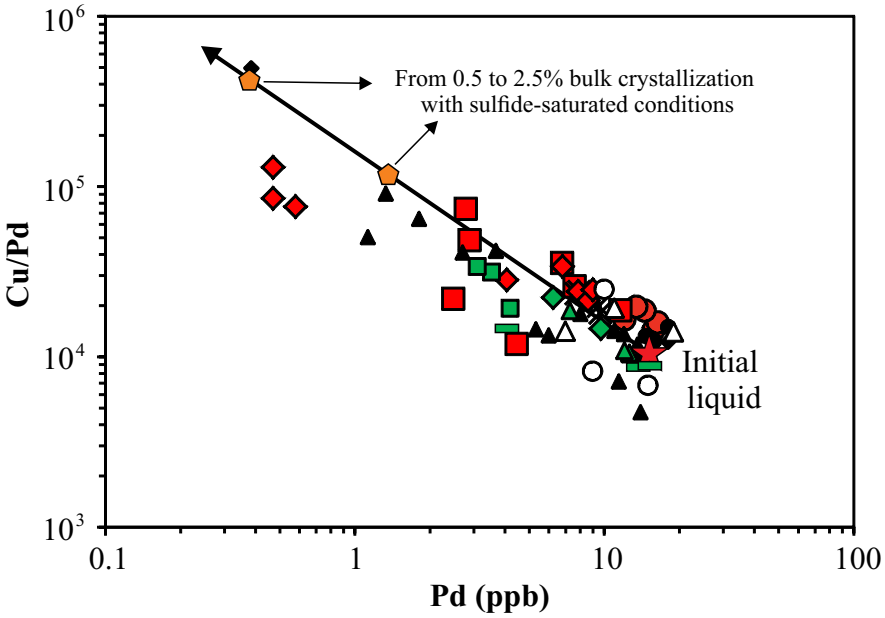

This study

High-Ti flows
- Pitanga type

Low-Ti flows
- Vale do Sol Fm.
- Torres Fm.
- Esmeralda Fm.
- Barros Cassal sequence

Ponta Grossa Arch
- Pitanga type
- Paranapanema type

Florianópolis Dyke Swarm
- Urubici type

Mincato (2000)

High-Ti flows
- Pitanga type
- Paranapanema type

Low-Ti flows
- Gramado type

Florianópolis dykes
- Urubici type

Barnes and Mansur

Etendeka Province
- Tafelberg Fm.
- Horingbaai Fm.

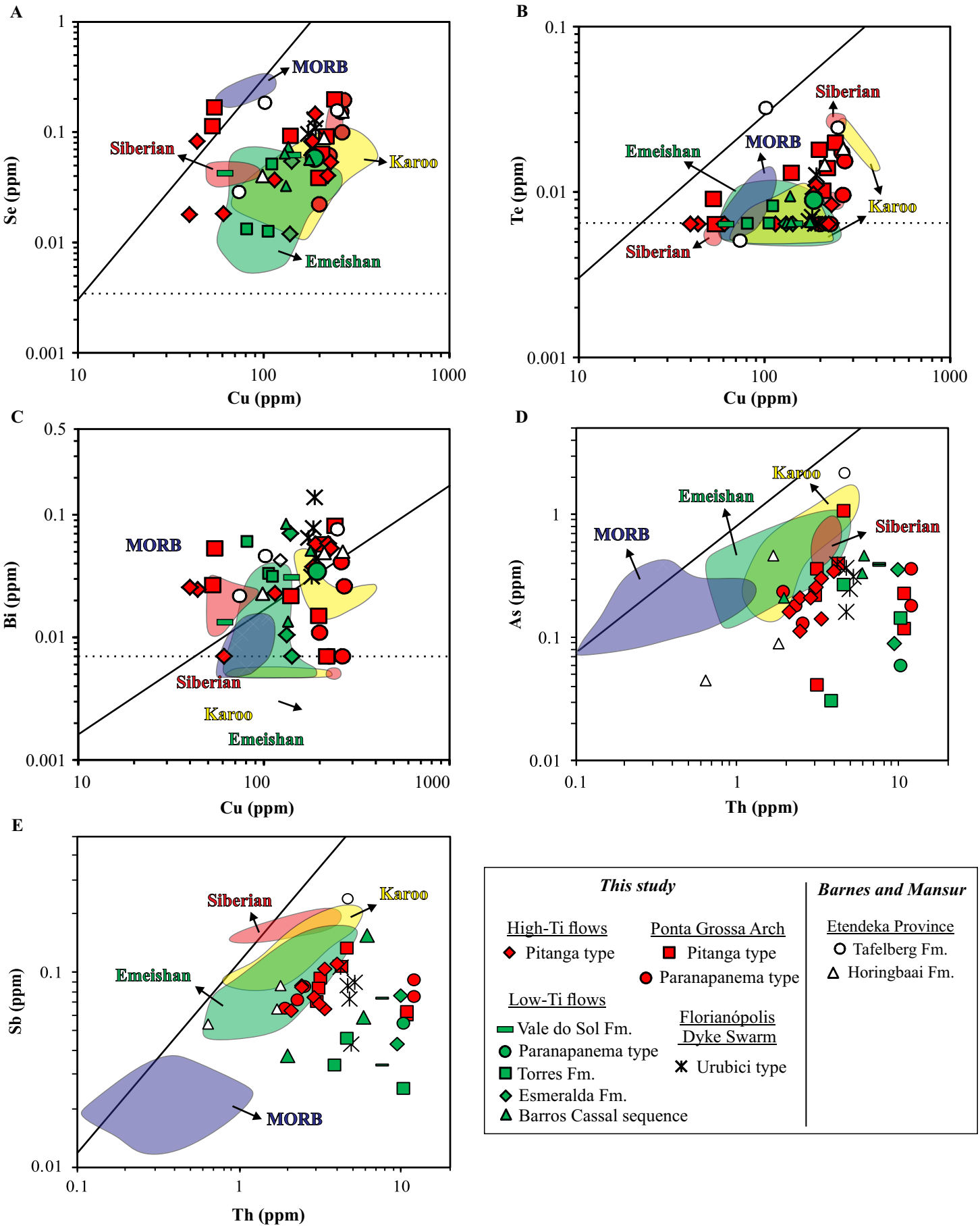
A
Se (ppm)
Cu (ppm)
MORB
Siberian
Karoo
Emeishan
B
Te (ppm)
Cu (ppm)
Siberian
Emeishan
MORB
Karoo
Siberian
C
Bi (ppm)
Cu (ppm)
MORB
Siberian
Karoo
Emeishan
D
As (ppm)
Th (ppm)
Karoo
Emeishan
MORB
Siberian
E
Sb (ppm)
Th (ppm)
Siberian
Karoo
Emeishan
MORB
This study
High-Ti flows
Pitanga type
Ponta Grossa Arch
Pitanga type
Paranapanema type
Low-Ti flows
Vale do Sol Fm.
Paranapanema type
Torres Fm.
Esmeralda Fm.
Barros Cassal sequence
Florianópolis Dyke Swarm
Urubici type
Barnes and Mansur
Etendeka Province
Tafelberg Fm.
Horingbaai Fm.

READ ME

Online Resource (ESM) for

The distribution of platinum-group elements and Te, As, Bi, Sb and Se (TABS+) in the Paraná Magmat fractionation, sulfide segregation and magma degassing

*Eduardo T. Mansur[1], Sarah-Jane Barnes[1], Valdecir Janasi[2], Renato Henrique-Pinto[2]; Adriana Alves[2]; Natas
Lithos

[1]Sciences de la Terre, Université du Québec à Chicoutimi, Québec, G7H 2B1, Canada
[2]Instituto de Geociências, Universidade de São Paulo, Brazil

*Corresponding author - E-mail address: etmansur@gmail.com

ic Province: Effects of crystal

ha Sarde Marteleto[2]

Table 1 - Whole-rock results used in this study.

Sample	Occurrence	Magma-type/Formation	Ru	Rh	Pd
			ppb	ppb	ppb
		Data Souce	**This work**		
Ponta Grossa Dyke Swarm - High-Ti					
as021	basaltic flow	Paranapanema type	0.18	0.49	15.77
as097a	basaltic flow	Pitanga type	**0.12**	0.17	2.48
as150	basaltic flow	Pitanga type	**0.12**	0.08	2.88
as202b	basaltic flow	Pitanga type	**0.12**	0.19	2.78
as296	basaltic flow	Paranapanema type	0.30	0.47	12.04
as552	basaltic flow	Pitanga type	**0.12**	0.15	7.59
gpl115a	dyke	Paranapanema type	0.19	0.40	16.41
gpl132a	sill	Pitanga type	**0.12**	0.08	4.45
gpl168	dyke	Paranapanema type	0.16	0.52	14.52
gpl179	sill	Pitanga type	**0.12**	0.08	5.34
gpl188	dyke	Paranapanema type	0.17	0.54	13.46
gpl190	dyke	Pitanga type	0.20	0.44	11.59
gpl192	sill	Pitanga type	0.14	0.25	6.77
Florianopolis Dyke Swarm					
CSC-01F	dyke	Urubici type	0.12	0.22	7.74
CSC-01G	dyke	Urubici type	0.12	0.29	9.65
VLF-31B	dyke	Urubici type	0.21	0.23	9.50
E-01F	dyke	Urubici type	0.19	0.24	8.91
E-24A	dyke	Urubici type	0.13	0.19	7.95
Northern high-Ti Basaltic Flows					
AQ-23	basaltic flow	Pitanga type	0.17	0.25	7.88
AQ-24A	basaltic flow	Pitanga type	0.18	0.33	8.62
AQ-25	basaltic flow	Pitanga type	0.16	0.40	9.01
AQ-35	basaltic flow	Pitanga type	0.17	0.24	6.81
IGN-83AA	basaltic flow	Pitanga type	0.12	0.08	0.58
IGN-83AC	basaltic flow	Pitanga type	0.12	0.08	0.47
AQ-12	basaltic flow	Pitanga type	0.18	0.15	4.08
AQ-42	basaltic flow	Pitanga type	0.12	0.08	0.47
Southern low-Ti Basaltic Flows					
RS-46	basaltic flow	Vale do Sol Fm.	0.21	1.05	15.50
RS-47	basaltic flow	Vale do Sol Fm.	0.16	0.50	13.83
RS - 71	basaltic flow	Esmeralda Fm.	0.15	0.33	9.71
RS 101	basaltic flow	Torres Fm.	0.15	0.34	3.54
RS 114	basaltic flow	Paranapanema type (south)	0.21	0.58	11.05
RS 121	basaltic flow	uncertain	0.25	0.39	13.03
GX-360B	dyke	Esmeralda Fm.	0.12	0.15	6.25
GX479	basaltic flow	Torres Fm.	0.12	0.23	3.14
GX486	basaltic flow	Barros Cassal sequence	0.23	0.46	12.48

GX489	basaltic flow	Barros Cassal sequence	0.18	0.43	13.01
XG-25	basaltic flow	Torres Fm.	0.18	0.57	4.20
XG-26	basaltic flow	Vale do Sol Fm.	0.15	0.38	4.10
XG-28	basaltic flow	Barros Cassal sequence	0.12	0.62	7.31
GX-417	basaltic flow	Barros Cassal sequence	0.14	0.48	11.63

PGE by Ni-fire assay and Te Co-percipitation, S by IR, As, Bi, Sb, Se, Te by HG-AFS, Bold fc
Sources of analyses: all trace-elements by ICPMS (values in italics) and major oxides and trace
Ponta Grossa Dyke swarm: Natasha Marteleto, Francisco Negri and Júlia Guerra
Florianópolis Dike Swarm: Natasha Marteleto and Luana Florisbal
Northern Basalt Flows: João Paulo Gusão
Southern Basalt Flows: Liza Polo

Os	Ir	Pt	Au	S	As	Sb
ppb	ppb	ppb	ppb	ppm	ppm	ppm
					This work	
0.07	0.11	8.51	2.58	61	0.174	0.072
0.07	0.03	4.99	3.93	771	0.389	0.107
0.07	0.03	4.57	1.23	**25**	0.348	0.094
0.07	0.06	5.25	7.65	215	0.216	0.070
0.10	0.10	10.36	2.09	**25**	0.228	0.066
0.07	0.07	15.99	1.62	**25**	0.040	0.083
0.07	0.06	12.64	2.08	260	0.352	0.091
0.07	0.03	4.64	0.85	213	1.037	0.133
0.07	0.07	16.30	2.15	371	0.127	0.084
0.07	0.03	7.12	1.04	1142	0.250	0.107
0.07	0.06	11.10	5.15	244	0.176	0.076
0.12	0.23	18.07	4.31	115	0.225	0.061
0.07	0.08	10.97	1.52	723	0.113	0.063
0.07	0.03	10.96	1.84	166	0.364	0.085
0.07	0.04	10.14	2.54	247	0.386	0.108
0.07	0.09	8.63	1.66	435	0.311	0.090
0.07	0.12	9.81	3.84	284	0.161	0.073
0.07	0.04	7.23	7.75	380	0.244	0.043
0.07	0.29	10.80	7.39	201	0.207	0.086
0.07	0.27	13.45	7.79	47	0.111	0.085
0.07	0.33	17.45	13.39	**25**	0.158	0.064
0.07	0.16	9.66	14.15	**25**	0.345	0.112
0.07	0.03	0.83	1.11	103	0.298	0.105
0.07	0.03	0.72	0.48	**25**	0.206	0.075
0.07	0.09	5.71	2.12	**25**	0.140	0.066
0.07	0.03	0.26	0.87	**25**	0.249	0.069
0.14	0.14	9.03	4.16	**25**	0.377	0.033
0.12	0.12	9.90	4.14	**25**		
0.10	0.08	5.42	0.64	**25**	0.090	0.043
0.07	0.07	7.07	7.01	**25**	0.139	0.025
0.10	0.07	9.04	3.87	**25**	0.057	0.054
0.09	0.11	14.92	5.82	**25**	0.112	0.023
0.07	0.03	5.44	3.04	**25**	0.356	0.076
0.07	0.04	4.96	8.55	**25**	0.262	0.046
0.09	0.06	11.41	3.61	**25**	0.189	0.056

0.07	0.07	9.55	7.68	**25**	0.211	0.038
0.11	0.04	5.89	2.29	**25**	0.030	0.033
0.09	0.06	7.62	6.96	**25**	0.387	0.073
0.09	0.08	8.31	1.39	**25**	0.324	0.059
0.07	0.05	10.92	0.85	**25**	0.460	0.155

ɔnt detection limits. Majors by XRF, trace elements by XFR (normal font) or ICP-MS italics
-elements by XFR from works supervised by Valdecir Janasi, with the participation of the following

Bi	Te	Se	**SiO2**	**TiO2**	**Ti**	**Al2O3**	**Fe2O3**
ppm	ppm	ppm	**%**	**%**	**%**	**%**	**%**
			??				
0.007	**0.006**	0.062	50.86	2.14	1.30	12.72	15.38
0.053	**0.006**	0.167	50.34	3.58	2.18	13.12	14.08
0.022	0.013	0.092	50.43	3.28	1.98	12.96	14.61
0.057	0.010	0.064	49.61	3.59	2.16	12.76	15.11
0.011	**0.006**	0.022	49.85	1.82	1.11	13.58	13.21
0.015	0.018	0.039	48.77	3.34	2.04	12.81	15.03
0.041	0.017	0.153	50.74	2.47	1.48	12.15	15.92
0.027	0.009	0.113	53.67	3.28	1.97	12.98	13.18
0.026	0.015	0.194	51.56	2.52	1.51	12.77	16.32
0.130	0.017	0.293	48.67	4.37		12.17	15.36
0.007	0.010	0.100	51.26	2.47	1.48	12.70	16.19
0.007	0.014	0.091	49.06	3.10	1.86	13.02	14.27
0.081	0.020	0.198	48.33	3.99	2.39	12.81	15.64
0.031	0.007	0.071	52.05	3.66	2.19	13.00	12.88
0.064	0.007	0.096	51.59	3.56	2.13	13.35	12.85
0.138	**0.006**	0.130	50.28	4.09	2.45	12.70	13.73
0.078	**0.006**	0.075	50.44	4.02	2.41	12.83	13.68
0.044	0.013	0.108	52.13	3.58	2.14	12.80	13.22
0.058	0.011	0.146	48.70	3.22	1.93	12.87	14.31
0.038	0.010	0.083	48.76	3.19	1.91	13.04	14.27
0.058	**0.006**	0.040	49.19	3.07	1.84	13.00	14.67
0.053	0.008	0.053	50.63	3.88	2.32	12.41	15.28
0.024	**0.006**	0.083	48.90	3.85	2.31	12.90	14.70
0.026	**0.006**	0.018	49.74	3.79	2.27	13.28	13.41
0.023	**0.006**	0.037	50.42	3.38	2.03	13.10	14.86
0.007	**0.006**	0.018	52.26	3.46	2.07	12.25	14.35
0.032	**0.006**	0.063	52.11	1.30	0.78	13.94	12.99
			52.15	1.30	0.78	13.98	13.02
0.007	**0.006**	0.054	49.80	1.39	0.84	13.73	13.67
0.031	0.008	0.051	53.59	1.07	0.64	14.08	11.64
0.035	0.009	0.061	50.62	2.01	1.20	13.19	14.68
0.007	0.011	0.154	49.41	1.26	0.76	13.74	12.73
0.070	**0.006**	0.012	51.12	1.43	0.86	14.44	14.68
0.033	**0.006**	0.013	52.18	1.16	0.69	13.64	11.91
0.080	**0.006**	0.063	49.71	1.21	0.72	13.73	13.14

0.013	0.009	0.072	50.02	1.22	0.73	13.86	13.01
0.061	**0.006**	0.013	52.75	1.00	0.60	15.87	9.23
0.014	**0.006**	0.043	57.05	1.57	0.94	13.07	13.36
0.010	**0.006**	0.031	54.10	1.39	0.83	13.50	12.62
0.048	**0.006**	0.055	54.17	1.88	1.12	12.15	15.65

researchers:

MnO	MgO	CaO	Na2O	K2O	P2O5	P	Loi	Total	Ba
%	%	%	%	%	%	%	%	%	ppm
0.22	4.86	9.37	2.34	0.68	0.24	0.10	0.85	99.66	*285*
0.20	4.36	8.14	2.90	1.48	0.51	0.22	1.11	99.82	*551*
0.25	4.65	8.61	2.78	1.39	0.37	0.16	0.01	99.34	*433*
0.25	4.74	8.99	2.64	1.30	0.43	0.19	0.16	99.58	*415*
0.20	6.19	10.66	2.19	0.48	0.20	0.09	0.76	99.13	*270*
0.22	4.90	9.07	2.52	1.00	0.39	0.18	0.36	98.41	*433*
0.23	5.04	8.88	2.30	0.96	0.26	0.11	0.00	98.95	254
0.19	3.58	7.26	2.95	2.04	0.56	0.25	0.20	99.89	*608*
0.23	4.18	8.84	2.48	0.99	0.30	0.13	0.00	100.18	*287*
0.22	4.37	7.61	3.15	1.40	0.48		1.09	98.88	< 37
0.23	4.63	9.10	2.27	1.02	0.28	0.12	0.00	100.14	330
0.21	5.38	9.49	2.27	0.93	0.34	0.15	1.48	99.55	484
0.19	4.55	8.61	2.27	1.08	0.44	0.19	1.27	99.18	250
0.16	4.14	7.82	3.01	1.84	0.56	0.24	< 0.01	99.12	*609*
0.16	4.20	8.19	2.75	1.87	0.53	0.23	0.04	99.09	*549*
0.17	4.04	7.58	2.73	2.19	0.60	0.26	0.66	98.77	*648*
0.19	4.33	7.91	2.59	1.97	0.57	0.25	0.68	99.21	*619*
0.17	3.94	7.48	2.98	2.06	0.58	0.25	0.61	99.54	*629*
0.19	5.50	9.66	2.25	0.87	0.35	0.15	1.43	99.36	585
0.18	5.13	9.84	2.20	0.84	0.36	0.16	1.95	99.76	304
0.20	5.58	9.77	2.32	1.06	0.32	0.14	0.56	99.74	315
0.23	4.08	7.79	2.64	1.76	0.64	0.28	0.17	99.51	537
0.21	4.62	8.64	2.51	1.18	0.57	0.25	1.23	99.31	480
0.17	4.92	8.66	2.57	1.50	0.50	0.22	1.07	99.60	449
0.21	4.66	8.54	2.58	1.53	0.41	0.18	0.42	100.11	458
0.21	4.21	7.93	2.20	1.25	0.48	0.21	1.07	99.66	533
0.20	5.64	9.47	2.54	0.99	0.18	0.08	0.20	99.55	273
0.20	5.49	9.36	2.78	1.22	0.18	0.08	0.32	100.00	297
0.19	6.54	10.36	2.30	0.58	0.16	0.07	1.23	99.96	284
0.19	5.98	9.69	2.23	1.00	0.12	0.05	0.30	99.89	216
0.20	5.38	9.35	2.44	1.06	0.23	0.10	0.66	99.82	295
0.20	7.18	11.18	2.48	0.32	0.11	0.05	1.46	100.07	*77*
0.17	4.75	7.33	2.24	0.70	0.18	0.08	2.50	99.54	296
0.18	5.57	8.51	3.25	1.62	0.17	0.07	0.93	99.12	*369*
0.18	6.62	10.60	2.17	0.52	0.13	0.06	0.52	98.53	156

0.19	6.72	10.55	2.18	0.74	0.13	0.06	0.48	99.10	*146*
0.15	5.26	9.26	1.96	1.05	0.18	0.08	3.22	99.94	*399*
0.19	3.05	6.60	2.57	2.33	0.21	0.09	0.42	100.42	*407*
0.17	4.25	8.03	2.60	1.74	0.20	0.09	0.53	99.13	*333*
0.21	2.95	6.90	2.57	2.08	0.28	0.12	0.44	99.27	*352*

Ce	Co	Cr	Cs	Cu	Dy	Er	Eu	Ga	Gd
ppm	ppm	ppm	ppm	ppm	ppm	ppm	ppm	ppm	ppm
44	40	43	*0.20*	226	*5.80*	*3.89*	*1.96*	20.4	*6.33*
85	31	21	*0.45*	54	*7.66*	*4.04*	*3.46*	24.2	*9.31*
64	39	44	*0.18*	139	*6.50*	*3.56*	*2.63*	22.6	*7.45*
68	36	76	*0.18*	206	*6.69*	*3.33*	*2.44*	22.8	*7.40*
37	44	152	*0.04*	200	*4.60*	*2.70*	*1.52*	18.5	*4.78*
67	41	66	*0.25*	198	*6.15*	*3.49*	*2.60*	20.9	*7.99*
44	42	61		261				21.0	
97	29	13	*0.62*	53	*8.77*	*4.05*	*3.32*	24.0	*9.79*
51	41	21	*0.22*	271	*6.73*	*3.92*	*2.05*	20.0	*6.60*
72	42	85		232				19.0	
48	47	31		265				21.0	
35	48	77		218				23.0	
37	41	60		241				21.0	
86	34	23	*2.02*	181	*6.86*	*3.35*	*3.11*	26.0	*9.11*
78	33	26	*2.97*	174	*6.37*	*3.17*	*3.01*	25.0	*8.47*
112	38	22	*1.75*	188	*8.69*	*4.03*	*3.85*	26.0	*11.08*
102	38	44	*1.77*	185	*7.83*	*3.58*	*3.57*	25.0	*10.19*
101	32	31	*0.95*	191	*8.01*	*3.75*	*3.51*	25.0	*10.19*
62	43	96	*0.60*	190	*5.95*	*2.88*	*2.24*	21.0	*6.87*
68	41	96	*0.52*	184	*5.80*	*2.88*	*2.17*	21.0	*7.20*
74	42	78	*0.09*	222	*5.55*	*2.58*	*1.99*	21.0	*6.29*
92	38	< 13	*0.32*	230	*9.31*	*4.25*	*3.06*	24.0	*9.68*
57	32	< 13	*0.22*	44	*7.32*	*3.68*	*3.17*	25.0	*9.50*
65	36	20	*0.15*	40	*7.14*	*3.08*	*2.78*	24.0	*8.38*
66	37	17	*0.17*	115	*6.93*	*3.15*	*2.56*	23.0	*7.89*
61	35	< 13	*0.53*	61	*7.48*	*3.50*	*2.82*	23.0	*9.17*
67	43	40		142				19.9	
50	41	37		126				19.1	
53	45	44		142				20.1	
< 35	40	78		111				20.2	
74	39	94		185				20.4	
64	41	218		98				19.4	
49	45	15		139				24.0	
47	42	31	*0.61*	106	*4.74*	*2.88*	*1.39*	20.0	*5.02*
< 35	43	89		131				18.0	

23	42	91	*3.22*	136	*4.01*	*2.60*	*1.17*	19.0	*4.07*
42	33	74	*0.86*	81	*3.96*	*2.31*	*1.27*	19.0	*4.17*
58	36	< 13	*2.35*	62	*6.19*	*3.72*	*1.69*	22.0	*6.26*
48	34	< 13	*2.54*	133	*5.63*	*3.40*	*1.54*	20.0	*5.54*
42	42	< 13	*3.72*	175	*6.32*	*3.71*	*1.68*	22.0	*6.23*

Hf	Ho	La	Lu	Mo	Nb	Nd	Ni	Pb	Pr
ppm	ppm	ppm	ppm	ppm	ppm	ppm	ppm	ppm	ppm
4.61	*1.37*	*21.3*	*0.52*	*1.44*	*11.8*	*21.8*	39.2	*3.01*	*4.89*
8.87	*1.58*	*42.5*	*0.48*	*1.66*	*25.1*	*46.8*	30.1	*5.04*	*10.30*
6.15	*1.36*	*31.0*	*0.47*	*1.16*	*18.8*	*34.4*	38.6	*4.11*	*7.94*
5.88	*1.28*	*30.8*	*0.45*	*1.26*	*18.6*	*37.6*	44.1	*4.17*	*8.86*
3.39	*0.96*	*16.8*	*0.39*	*1.01*	*9.8*	*20.2*	82.5	*2.87*	*4.64*
5.94	*1.27*	*31.0*	*0.43*	*1.36*	*19.1*	*34.1*	58.7	*3.92*	*8.08*
					17.0	30.0	58.0		
9.32	*1.65*	*44.6*	*0.53*		*29.1*	*58.5*	31.0	*5.99*	*12.80*
5.31	*1.47*	*22.7*	*0.53*		*13.0*	*27.9*	41.0	*3.29*	*6.29*
					18.0	34.0	66.0		
					18.0	24.0	49.0		
					19.0	33.0	73.0		
					21.0	29.0	57.0		
7.90	*1.28*	*39.9*	*0.35*		*37.5*	*45.1*	42.0	*7.13*	*12.31*
7.50	*1.21*	*35.7*	*0.33*		*35.6*	*41.8*	47.0	*10.13*	*11.24*
9.20	*1.70*	*51.7*	*0.44*		*28.2*	*60.7*	56.0	*7.18*	*14.50*
8.23	*1.52*	*47.6*	*0.39*		*28.4*	*54.8*	63.0	*7.19*	*13.19*
8.31	*1.59*	*47.0*	*0.42*		*30.9*	*54.5*	52.0	*6.11*	*12.94*
5.19	*1.13*	*26.3*	*0.36*		*18.5*	*32.5*	83.0	*3.33*	*7.27*
5.10	*1.11*	*26.1*	*0.34*		*18.6*	*32.9*	74.0	*3.43*	*7.87*
4.62	*1.01*	*22.8*	*0.32*		*16.8*	*32.2*	73.0	*3.20*	*7.20*
7.95	*1.77*	*40.1*	*0.66*		*27.3*	*54.6*	48.0	*5.28*	*12.00*
7.33	*1.47*	*37.2*	*0.41*		*26.5*	*46.1*	34.0	*4.40*	*10.10*
6.50	*1.38*	*32.3*	*0.40*		*23.4*	*43.9*	37.0	*3.87*	*9.43*
6.36	*1.29*	*34.0*	*0.42*		*22.6*	*43.4*	47.0	*4.64*	*9.66*
6.68	*1.36*	*32.8*	*0.42*		*22.2*	*44.6*	32.0	*4.94*	*10.50*
					9.6	35.7	45.5		
					9.1	48.7	46.1		
					7.9	42.1	44.6		
					< 9	42.0	44.4		
					12.3	44.9	57.3		
					< 9	24.8	86.1		
					12.0	30.0	43.0		
3.82	*1.00*	*21.3*	*0.41*		*10.2*	*23.5*	45.0	*6.88*	*5.99*
					< 9	< 14	68.0		

2.53	*0.93*	*10.2*	*0.35*	*5.0*	*13.2*	69.0	*3.12*	*2.97*
3.30	*0.83*	*19.7*	*0.32*	*9.0*	*21.1*	66.0	*8.45*	*5.72*
5.15	*1.33*	*27.1*	*0.53*	*14.8*	*29.5*	9.0	*12.53*	*8.00*
4.11	*1.23*	*22.9*	*0.47*	*13.0*	*24.8*	31.0	*9.75*	*6.64*
4.00	*1.34*	*22.0*	*0.52*	*15.6*	*25.8*	29.0	*9.00*	*6.02*

Rb	Sc	Sm	Sr	Ta	Tb	Th	Tm	U	V
ppm	ppm	ppm	ppm	ppm	ppm	ppm	ppm	ppm	ppm
18.6	*41.2*	*5.72*	*318*	*0.86*	*0.92*	*2.31*	*0.51*	*0.41*	457
37.3	*24.3*	*11.00*	*463*	*1.83*	*1.32*	*4.32*	*0.48*	*0.82*	402
37.3	*29.7*	*7.88*	*412*	*1.38*	*1.14*	*3.19*	*0.48*	*0.61*	496
37.3	*30.9*	*7.93*	*434*	*1.44*	*1.21*	*3.08*	*0.49*	*0.61*	435
37.3	*39.2*	*4.67*	*307*	*0.68*	*0.78*	*1.96*	*0.39*	*0.34*	372
37.3	*30.7*	*7.92*	*390*	*1.33*	*1.10*	*3.15*	*0.46*	*0.62*	520
29.0	40.0		215						452
43.9	*24.2*	*12.80*	*502*		*1.51*	*4.64*	*0.55*	*0.95*	323
21.4	*40.9*	*7.08*	*241*		*1.09*	*2.57*	*0.53*	*0.46*	401
18.0	36.0		358						320
17.0	37.0		263						460
12.0	32.0		476						417
38.0	33.0		338						386
38.4	25.0	*9.80*	*677*		*1.31*	*4.73*	*0.42*	*1.03*	323
40.4	25.0	*9.19*	*696*		*1.20*	*4.17*	*0.39*	*0.93*	315
139.7	27.0	*12.68*	*756*		*1.61*	*5.22*	*0.55*	*1.10*	350
73.3	26.0	*11.57*	*738*		*1.45*	*4.74*	*0.48*	*0.99*	343
45.5	25.0	*11.72*	*680*		*1.48*	*4.97*	*0.50*	*0.97*	297
24.3	*30.4*	*7.12*	*474*		*1.03*	*2.44*	*0.40*	*0.53*	422
23.4	*30.1*	*6.96*	*487*		*1.09*	*2.43*	*0.44*	*0.55*	436
18.7	*30.2*	*6.33*	*494*		*1.03*	*2.09*	*0.40*	*0.46*	432
36.5	*27.5*	*11.40*	*482*		*1.57*	*3.99*	*0.66*	*0.83*	401
23.7	*27.0*	*10.10*	*564*		*1.30*	*3.37*	*0.48*	*0.71*	403
26.7	*27.0*	*9.27*	*560*		*1.25*	*2.89*	*0.43*	*0.63*	409
29.3	*28.7*	*8.64*	*499*		*1.21*	*3.34*	*0.46*	*0.68*	460
43.6	*25.8*	*9.00*	*523*		*1.45*	*3.11*	*0.55*	*0.72*	389
30.4	35.4		221						346
38.4	38.0		210						529
7.8	38.4		196						379
32.4	36.3		209						293
23.6	37.3		255						384
10.1	41.0		151						339
35.0	40.0		210						382
53.5	*35.1*	*4.84*	*232*		*0.85*	*4.68*	*0.44*	*0.76*	266
14.0	36.0		183						328

42.8	*37.6*	*3.46*	*171*		*0.69*	*1.97*	*0.37*	*0.46*	334
24.6	31.0	*4.40*	*367*		*0.68*	*3.91*	*0.34*	*1.03*	236
87.6	33.0	*6.49*	*199*		*1.07*	*7.76*	*0.57*	*1.78*	374
69.6	31.0	*5.57*	*213*		*0.96*	*5.92*	*0.52*	*1.55*	329
96.5	32.0	*5.74*	*158*		*1.03*	*6.16*	*0.56*	*1.54*	464

Y	Yb	Zn	Zr
ppm	ppm	ppm	ppm
34.7	*3.12*	117	*177*
38.6	*3.05*	128	*349*
34.5	*3.08*	132	*240*
34.2	*3.07*	167	*246*
26.0	*2.42*	176	*137*
33.0	*2.68*	126	*246*
41.0		120	178
47.1	*3.58*	124	*381*
39.9	*3.38*	125	*206*
40.0		119	193
39.0		127	184
54.0		113	194
37.0		125	184
35.2	*2.51*	119	*283*
32.8	*2.38*	130	*271*
41.4	*3.07*	121	*356*
39.1	*2.64*	165	*322*
39.8	*2.88*	110	*327*
29.9	*2.51*	109	*210*
29.7	*2.61*	115	*213*
27.9	*2.57*	108	*193*
45.8	*4.43*	129	*326*
37.7	*2.86*	127	*306*
34.6	*2.71*	119	*271*
33.8	*2.94*	118	*267*
36.9	*3.33*	126	*279*
27.8		95	120
27.0		93	119
28.2		95	123
23.9		89	100
32.3		113	157
24.3		93	74
37.0		117	154
26.8	*2.77*	94	*146*
26.0		86	100

24.7	*2.22*	86	*91*
21.7	*2.03*	73	*129*
34.3	*3.32*	112	*193*
32.0	*2.99*	94	*160*
40.1	*3.62*	124	*178*

Table 2 - Analyses of reference materials used to monitor the data quality of HG-AFS analyses.

			As ppm	Bi ppm	Sb ppm	Se ppm
Detection limits			0.003	0.007	0.009	0.003
Name	CH 4	Certificate value*	8.80	0.60	0.77	2.10
Rock Type	Anorthosite	Stdev	0.60	0.20	0.40	0.20
Source	CANMET	This study	8.29	0.50	0.74	1.98
		Stdev (n= 6)	0.45	0.06	0.07	0.15
		Relative stdev %	5.44	11.09	9.74	7.72
Name	TDB-1	Certificate value*	2.50	*0.063*	1.00	*0.38*
Rock Type	Diabase	Stdev	0.50	*0.019*	0.40	*0.03*
Source	CANMET	This study	1.95	0.090	0.90	0.35
		Stdev (n= 6)	0.15	0.019	0.08	0.05
		Relative stdev %	7.44	21.11	8.64	13.04
Name	OKUM	Certificate value*	*0.24*	*0.072*	*0.111*	*0.101*
Rock Type	Komatiite	Stdev	0.03	0.009	0.013	0.009
Source	IAG	This study	0.27	0.093	0.093	0.090
		Stdev (n= 6)	0.03	0.019	0.011	0.010
		Relative stdev %	12.23	20.53	11.84	11.14

Detection limit = 3*sigma of the blank

*Normal font certificate or assigned value, italics average of literature values and Mansur et al. (2(

Stdev = standard deviation; Relative stdev= relative standard deviation; n= number of individual a

Te ppm
0.006
0.36
0.07
0.33
0.04
13.11
0.04
0.01
0.03
0.01
34.62
0.053
0.005
0.035
0.012
34.69

)20a) for
ınalyses

Table 3 - Analyses of reference materials used to monitor the data quality of PGE, Au and S analyses.

		Ru ppb	Rh ppb	Pd ppb	Os ppb	Ir ppb
Ref Material	Detection limits	0.12	0.08	0.47	0.07	0.03
OKUM	Certificate value	4.25	1.40	11.70		0.99
Abitibi	Stdev	0.30	0.13	0.50		0.07
komatiite	This study	4.53	1.53	12.75	<dl	1.07
IAG	Stdev (n= 3)	0.16	0.03	0.48		0.02
	Relative stdev	3.48	1.85	3.75		1.63
LK-NIP-1	Certificate value	0.44	0.90	17.96		0.19
Diabase	Stdev					
Geolabs	This study	0.54	1.00	18.70	<dl	0.17
	Stdev (n= 3)	0.02	0.09	0.77		0.02
	Relative stdev	4.21	8.57	4.14		13.78
KPT-1	Certificate value	17.30	17.10	122.00	2.80	6.80
Sudbury	Stdev	2.00	1.10	17.00	0.60	1.50
Dolerite dyke	This study	18.27	17.29	143.17	3.28	6.63
IAG	Stdev (n= 3)	0.27	0.46	20.08	0.50	0.27
	Relative stdev	1.48	2.64	14.02	15.18	4.10
LDI	Certificate value	0.31	0.69	939.26	2.80	0.07
Lac des Iles	Stdev	0.03	0.04	35.41	0.60	0.01
Gabbronorite	This study	0.40	0.82	980.12	2.34	0.15
Geolabs	Stdev (n= 3)	0.04	0.20	13.98	0.86	0.08
	Relative stdev	10.08	23.90	1.43	36.71	53.33

Detection limit = 3*sigma of the blank

Stdev = standard deviation; Relative stdev= relative standard deviation; n= number of individual analy

Values for PGE and Au in ppb. Values for S in ppm.

Pt ppb	Au ppb	S ppm
0.08	0.48	25
11.00	1.49	240
0.60	0.16	
12.12	0.77	265
0.87	0.54	
7.16	70.17	
13.43	4.63	200
14.72	5.14	225
0.35	1.49	
2.39	29.01	
97.40	41.10	10293
20.10	21.30	341
114.52	40.94	
33.92	10.12	10188
29.62	24.73	
100.46	63.00	
10.87	17.91	
119.51	80.22	
5.64	1.82	
4.72	2.27	

yses

Table 4 - Analyses of reference materials used to monitor the data quality of whole-rock analyses of maj

		SiO2	TiO2	Al2O3	Fe2O3	MnO	MgO	CaO
JB 1a	This study	52.60	1.284	14.46	9.05	0.148	7.81	9.37
	Certificate value	52.160	1.3	14.51	9.10	0.15	7.75	9.23
JG 1a	This study	72.03	0.234	14.23	2.00	0.060	0.77	2.13
	Certificate value	72.19	0.25	14.22	2.05	0.06	0.69	2.13

or oxides and trace elements. Values for major oxides in percentage. Values for trace elements in ppm.

Na2O	K2O	P2O5	LoI	Total	Ba	Ce	Co	Cr
2.84	1.40	0.258	1.1	100.32	495	86	37	420
2.74	1.42	0.26	1.1	99.72	497	66.1	39.5	415
3.53	4.00	0.090	0.59	99.66	430	43	< 6	23
3.41	4.01	0.08	0.59	99.68	458	45.2	5.7	18.6

Cu	Ga	La	Nb	Nd	Ni	Pb	Rb	Sc	Sr	Th
56	17	40	25	30	144	5	39	30	437	10
55.5	18	38.1	27	25.5	140	7.2	41	27.9	443	8.8
< 5	16	< 28	11	21	< 5	38	169	< 14	170	15
1.3	17	21.8	12	21	6.4	27	180	6.31	185	12.1

U	V	Y	Zn	Zr	F
6	200	23	81	135	461
1.6	220	24	82	146	385
13	22	27	37	111	695
4.7	23	31.6	38.8	121	450